Perimeter Modes of Nanomechanical Resonators Exhibit Quality Factors Exceeding 10^9 at Room Temperature

Mohammad J. Bereyhi⊙,[*] Amirali Arabmoheghi,[*] Alberto Beccari⊙, Sergey A. Fedorov, Guanhao Huang,
Tobias J. Kippenberg,[†] and Nils J. Engelsen⊙[‡]

Institute of Physics (IPHYS), Swiss Federal Institute of Technology Lausanne (EPFL),
1015 Lausanne, Switzerland

Systems with low mechanical dissipation are extensively used in precision measurements such as gravitational wave detection, atomic force microscopy, and quantum control of mechanical oscillators via optomechanics and electromechanics. The mechanical quality factor (Q) of these systems determines the thermomechanical force noise and the thermal decoherence rate of mechanical quantum states. While the dissipation rate is typically set by the bulk acoustic properties of the material, by exploiting dissipation dilution, mechanical Q can be engineered through geometry and increased by many orders of magnitude Recently, soft clamping in combination with strain engineering has enabled room temperature quality factors approaching 10^9 in millimeter-scale resonators. Here we demonstrate a new approach to soft clamping which exploits vibrations in the perimeter of polygon-shaped resonators tethered at their vertices. In contrast to previous approaches, which rely on cascaded elements to achieve soft clamping, perimeter modes are soft clamped due to symmetry and the boundary conditions at the polygon vertices. Perimeter modes reach Q's of 3.6×10^9—a record at room temperature—while spanning only two acoustic wavelengths. We demonstrate thermal-noise-limited force sensitivity of 1.3 aN/$\sqrt{\text{Hz}}$ for a 226 kHz perimeter mode with quality factor of 1.5×10^9 at room temperature. The small size of our devices makes them well suited for near-field integration with microcavities for quantum optomechanical experiments. Moreover, their compactness allows the realization of phononic lattices. We demonstrate a one-dimensional Su-Schrieffer-Heeger chain of high-Q perimeter modes coupled via nearest-neighbour interaction and characterize the localized edge modes.

Subject Areas: Condensed Matter Physics, Mechanics
Nanophysics

I. INTRODUCTION

High-Q mechanical resonators have found widespread application in precision measurements, including interferometric detection of gravitational waves [1] and optomechanical experiments exploring the limits of quantum measurement [2–5]. In these endeavors, mechanical dissipation plays a central role as it describes the coupling rate to the thermal bath, and together with the resonator's effective mass sets the thermal force noise floor [6,7]. High force sensitivity requires low mass and low dissipation and one typically comes at the cost of the other, as

mechanical losses are often dominated by surface effects, and it has therefore been observed that smaller mechanical resonators have higher dissipation [8].

Over the past decade, the experimentally accessible quality factors of nanomechanical resonators have increased by 3 orders of magnitude. This revolution in dissipation control is underpinned by the phenomenon "dissipation dilution," first seen in test mass suspensions of gravitational wave detectors [1]. Dissipation dilution occurs through a combination of stress and geometric nonlinearity [9], the condition where resonator elongation is quadratic in mode amplitude. Notably, dissipation dilution allows reduction of dissipation by engineering the geometry of the resonator rather than its constituent materials. It was shown that in the regime of strong dissipation dilution, most of the mechanical losses of an unpatterned structure arise from mode curvature near the boundaries [10,11]. A number of techniques were therefore developed which reduce the mechanical mode amplitude near the clamping points, including phononic band gap engineering [11], clamp tapering [12], and
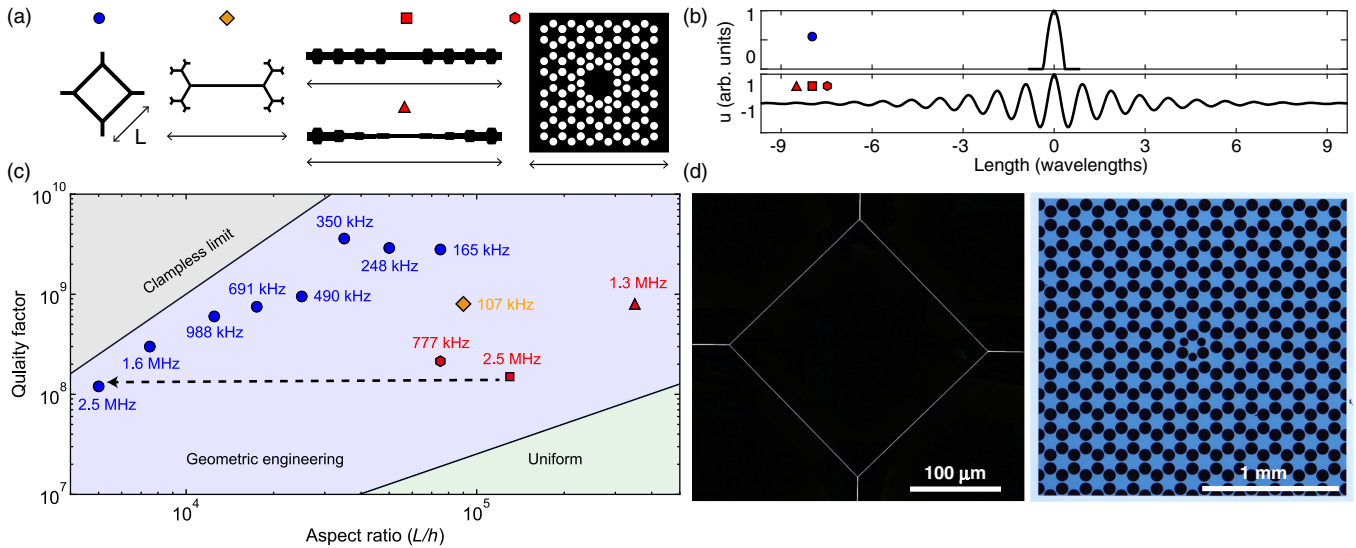
FIG. 1.   Comparison of state-of-the-art strained mechanical resonator designs. (a) Schematics of different mechanical resonators with their spatial extent illustrated by double-headed arrows (L). From left to right: polygon resonator, binary tree nanobeam [13], phononic crystal nanobeam [15], strain engineered nanobeam [15], and phononic crystal membrane [11]. (b) Simulated displacement profile of perimeter modes (plotted between two adjacent clamps) and phononic crystal soft-clamped modes with the same frequency. (c) Measured room temperature Q for polygons (blue circles) with different aspect ratios (L/h) and the best reported values for other designs of tensioned resonators [11,13,15]. For each data point, the corresponding resonance frequency is written on the plot. The green shaded area is accessible for the fundamental mode of a tensioned nanobeam with 20 nm thickness (h). The solid black line separating the gray and blue shaded areas shows the clampless limit for a 20-nm-thick beam [Eq. (2)]. The dashed arrow compares a polygon ($Q = 120 \times 10^6$) and a phononic crystal soft-clamped beam ($Q = 150 \times 10^6$) with the same thickness ($h = 20$ nm) and frequency ($f = 2.5$ MHz), showing 26 times lower aspect ratio for the polygon resonator, given the particular number of unit cells ($n = 26$) chosen for the phononic crystal soft-clamped beam in Ref. [15]. (d) Size comparison between a 200-μm-long polygon resonator with $Q = 155 \times 10^6$ at 1.6 MHz and a 2×2 mm^2 phononic crystal membrane with $Q = 74 \times 10^6$ at 1.46 MHz frequency [22], illustrating the reduced size.

hierarchical structuring [13,14]. The elimination of these boundary losses (soft clamping [11]) has allowed nanomechanical resonators with quality factors of nearly 10^9 at room temperature [15], approaching cryogenically cooled single crystal quartz ($Q = 8 \times 10^9$) and bulk sapphire resonators ($Q > 10^9$) [16,17].

To realize high mechanical quality factors by dissipation dilution, extremely high aspect ratios (i.e., length/thickness $> 10^5$) are required: state-of-the-art implementations have thicknesses of tens of nanometers and lengths on the millimeter scale [11,13,15,18]. For example, phononic band gap engineering typically requires a structure size of at least ten acoustic wavelengths. These large sizes present an obstacle to the practical use of such resonators in integrated optomechanical systems, where the mechanical resonator is suspended within hundreds of nanometers from an optical microcavity to engineer strong near-field optomechanical coupling [19,20]. The large size requirement also limits the attainable quality factors in such resonators due to the difficulty of suspending stressed resonators larger than a few millimeters.

We realized mechanical resonators with quality factors exceeding 3×10^9 at room temperature, surpassing the state-of-the-art mechanical Q factors [15] by a factor of 4 in

tenfold smaller devices [Fig. 1(c)]. These structures are well suited for integration with nanoscale cavities for sensing and quantum optomechanical experiments. The simplicity of the design further increases its flexibility: by scaling the size of the resonator, soft-clamped perimeter modes can be realized at different frequencies. In our work, we show $Q > 10^8$ over a span of more than four octaves (170 kHz–2.5 MHz), but smaller and larger frequencies are also possible. We perform efficient displacement readout of the perimeter modes using a free-space optical interferometer and demonstrate thermal-limited force sensing enabled by feedback damping [21].

The perimeter modes of different polygon resonators can be coupled through a joint tether, allowing the creation of phononic dimers. Phononic dimers have been studied in defect modes of phononic crystals [23–26], targeting force sensing applications [27–29]. The compactness of the resonators also simplifies the creation of large, coupled phononic arrays, making polygon resonators a suitable platform for exploring multimode physics of phononic structures, such as topological modes [30–35]. As a proof of principle, we demonstrate a one-dimensional array of six resonators forming a Su-Schrieffer-Heeger (SSH) chain [36] and characterize the localized edge modes. Moreover,

coupling these arrays to optical cavities could allow experimental implementation of two-mode mechanical entanglement protocols [37].

II. SOFT-CLAMPED PERIMETER MODES

The quality factor of a mechanical mode experiencing dissipation dilution is enhanced by the dilution factor (D_Q) [9] over the intrinsic quality factor of the material (Q_{int}) such that $Q = D_Q \times Q_{int}$. The intrinsic quality factor is a material property, given by $Q_{int} = 1/\phi$, where ϕ is the loss angle characterizing the delay between stress and strain. D_Q can be engineered by changing the resonator geometry, and here we show that perimeter modes have 2 orders of magnitude higher D_Q compared to uniform strings.

Our resonators can be understood as a network of tensioned one-dimensional strings. It is therefore useful to start from the dilution factor of the nth flexural mode of a stressed mechanical resonator [1,9,38]:

$$D_{Q,n} = \frac{1}{\alpha_n \lambda + \beta_n \lambda^2}, \qquad \lambda = \sqrt{\frac{1}{12\epsilon}} \frac{h}{l}, \qquad (1)$$

with thickness h, characteristic length l, and average strain ϵ. The $\alpha_n \lambda$ term arises from the curvature near the boundaries and $\beta_n \lambda^2$ from the curvature distributed over the rest of the mode. For structures with high tension and large aspect ratio, λ is much smaller than one, and α_n therefore sets the limit on the dilution factor. If we consider a structure with no boundary curvature [$\alpha_n = 0$ in Eq. (1)], the D_Q for a given strain is bounded by

$$D_Q \leq \frac{12E\epsilon^2}{\rho h^2 \omega^2}, \qquad (2)$$

where ρ is the film density, ω the mechanical mode frequency, and E the Young's modulus of the material [9]. The limit in Eq. (2) corresponds to the dilution factor experienced by the fundamental mode ($n = 1$) of a hypothetical, clampless beam ($1/\beta_1 \lambda^2$) vibrating at frequency ω. We call this limit the "clampless" limit for the quality factor.

The boundary curvature (α_n) can be suppressed by soft-clamping techniques, two of which were previously reported: phononic band gap engineering [11,15] and hierarchical structuring [13]. While hierarchically structured resonators [13,14] are prevented from reaching the clampless limit by torsional losses, phononic band gap engineering allows one to saturate Eq. (2) at the cost of larger device size [11,15]. In the following, we show that a different class of resonators also host soft-clamped modes and approach the clampless limit: polygons composed of connected beams that are tethered at their vertices. Figure 2(a) shows an example polygon resonator with four vertices and the simulated displacement profile of its fundamental perimeter mode, i.e., the mode which has half an acoustic wavelength per polygon side. Figure 2(b) shows fabricated polygon resonators with four, six, and eight vertices.

The dissipation dilution of perimeter modes of polygon resonators can be found analytically under the narrow-beam approximation, in which the length over width ratios of all constituent beams are infinitely large. In this case, the boundary loss coefficient (α_n) is zero, since perimeter
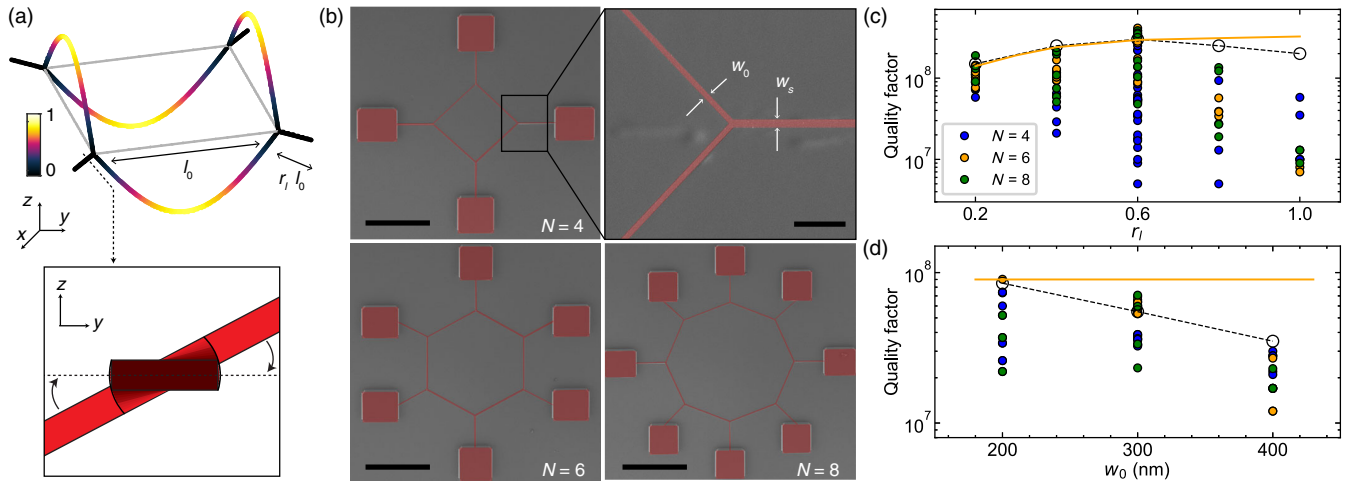

FIG. 2. Ultrahigh-Q perimeter modes. (a) FEM simulation of the fundamental perimeter mode with an inset showing the generation of torsional deformation of the tethers. (b) False-colored scanning electron micrographs of polygon Si_3N_4 strained resonator devices with $l_0 = 700$ μm, $r_l = 0.6$, $w_0 = 200$ nm, and 20 nm thickness (scale bars correspond to 500 μm). Top right of (b) shows an enlarged junction of a stress-preserving square resonator (scale bar corresponds to 1.5 μm). (c) The effect of tether length (r_l) on Q for samples with $l_0 = 250$ μm, $w_0 = 300$ nm, and 20 nm thickness. Blue, orange, and green data points represent square, hexagon, and octagon resonators, respectively. (d) The effect of polygon width (w_0) on the Q for samples with $l_0 = 100$ μm, $r_l = 0.6$, and 20 nm thickness. Open circles (joined by a dashed line) are FEM simulations and orange line is the Q computed from Eq. (3).

modes do not produce flexural displacements in the tethers. The torsional deformations of the tethers, however, are always non-negligible, and they add to the distributed loss coefficient β_n.

The dilution factor equals the ratio of the tension energy stored by the sinusoidal standing waves in the perimeter beams to the sum of the bending energy of those waves and the torsional energy of the tethers. For an N-sided polygon with equal stress along all segments, D_Q^{-1} is found as

$$D_Q^{-1} = \left(\frac{1}{n^2\pi^2\lambda^2}\right)^{-1} + \left(\frac{r_l(1+\nu)\cos^2{(\pi/N)}}{4r_w\lambda^2}\right)^{-1}, \quad (3)$$

where r_l is the ratio of the support length to the side length of the polygon [Fig. 2(a)], $r_w = w_s/w_0$ is the ratio of the support width to the side width of the polygon, n is the perimeter mode order, and ν is the Poisson ratio of the material (see Appendix A). Equation (3) shows that torsional losses prevent the dilution factor of the fundamental perimeter mode [$n = 1$, as illustrated in Fig. 2(a)] from saturating Eq. (2).

The predictions of Eq. (3) are in good quantitative agreement with experimental results for a subset of devices

in our work, namely the ones with the highest length-to-width aspect ratio as shown in Figs. 2(c) and 2(d) (also see Appendix A). For the others, it still provides qualitative insights, but we resort to two-dimensional finite-element simulations for quantitative theoretical predictions. The validity range of Eq. (3) is investigated in detail in Appendix A. One qualitatively new effect introduced by finite aspect ratio is a finite boundary loss coefficient (α_n), which in real structures is suppressed by a factor of order $(w_s/l_s)^2$, where l_s is the length and w_s is the width of the supports. Additionally, the dependence of Q on width that we observe in FEM simulations is not captured by this simple model, as it arises due to the torsional deformations of the polygon sides.

III. EXPERIMENTAL CHARACTERIZATION OF PERIMETER MODES

We fabricate devices out of 20-nm-thick Si_3N_4 film with 1 GPa deposition stress, following a previously established fabrication process focused on creating large gaps between the suspended resonators and the substrate [39] (see Appendix D). The intrinsic quality factor of the film has
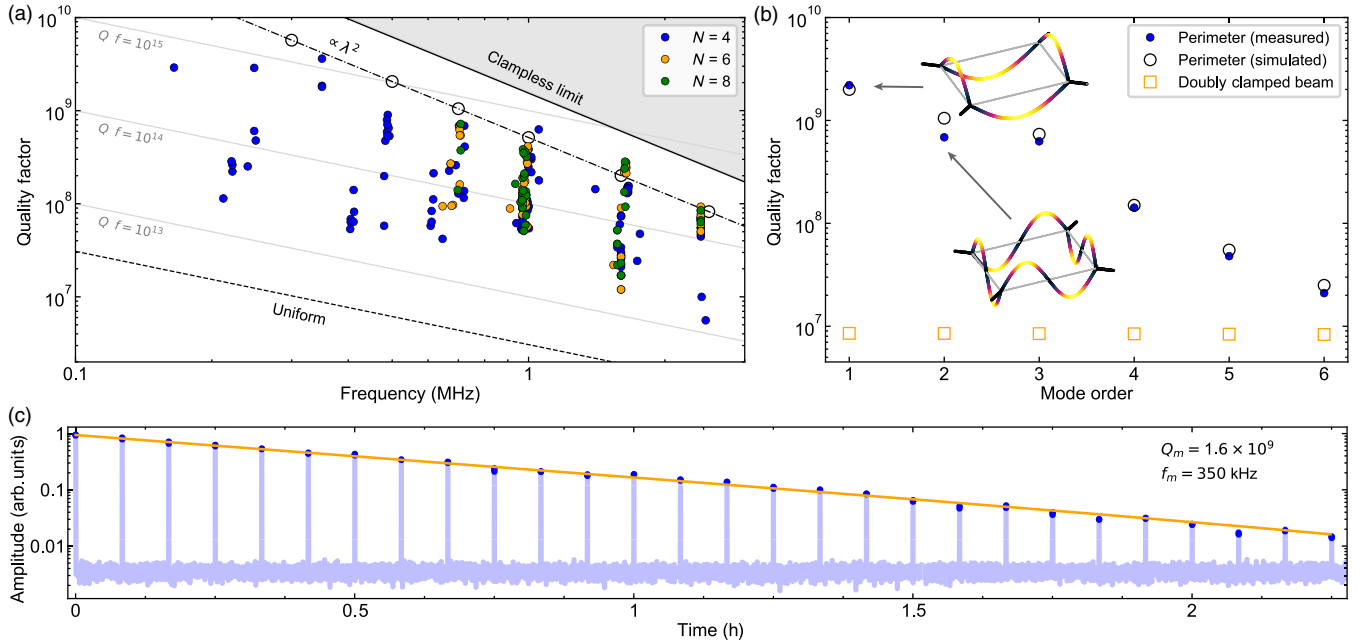

FIG. 3. Characterization of fundamental and higher-order perimeter modes. (a) A survey of all the measured Q's of fundamental perimeter modes for square-, hexagon-, and octagon-shaped Si_3N_4 resonators (blue, orange, and green circles, respectively), with $r_l \in [0.2, 0.4, 0.6, 0.8]$ and $w_0 = 200$ and 300 nm. The solid black line shows the clampless limit for a 20 nm Si_3N_4 film assuming intrinsic quality factor of $Q_{int} = 2500$. FEM simulation Q's (open circles) are plotted for optimal geometrical parameters ($r_l = 0.6$ and $w_0 = 200$ nm). The dot-dashed line interpolates the FEM simulation Q's and shows the λ^2 scaling. The dashed line is the fundamental mode Q of a uniform nanobeam. (b) High-order perimeter mode Q's (blue dots) of a square with $l_0 = 700$ μm, $r_l = 0.2$, and $w_0 = 200$ nm are shown with FEM predictions (open circles). Open squares show the calculated Q's of a uniform beam with the same thickness and fundamental mode frequency. Displacement profiles of the first two perimeter modes are shown as insets. (c) Gated ringdown measurement (1 s on, 5 min off) of a square with $l_0 = 700$ μm, $r_l = 0.2$, and $w_0 = 200$ nm with a fundamental perimeter mode Q of 1.6×10^9 at 350 kHz. Orange line: exponential fit to the data shown by blue circles. Faded blue data are excluded from the fit as the laser is blocked at these times.

been previously characterized to be $Q_{int} = 2500$ [13] and we use this value to compute the predicted Q after finding D_Q using FEM simulations or theoretical modeling. Mechanical Q's are extracted from ringdown decay times of excited modes measured using a free-space optical interferometer with gated laser illumination of the sample [see Fig. 4(d) and Ref. [13] for more details]. An example ringdown trace is shown in Fig. 3(c). The chips are rested on a holder inside the vacuum chamber without any fixation unless otherwise indicated. We investigate the effect of chip mounting on the Q in detail in Appendix F, where we find that perimeter modes are less sensitive to chip clamping conditions than the low order modes of unpatterned nanobeams [38] and membranes [40].

We first investigate the dependence of Q on the relative support length (r_l). We expect an initial increase in Q as a function of support length due to the reduction of lossy torsional energy. However, as r_l reaches one, torsional modes of the supports start to hybridize with the perimeter modes leading to a dramatic increase in dissipation (see Appendix A). This is reflected in FEM simulations and measurements, with a decrease in Q starting from $r_l = 0.8$ [see Fig. 2(c)]. We next investigate the influence of overall resonator width (w_0) by fabricating and characterizing polygons with varying widths and $l_0 = 100$ μm and $r_l = 0.6$ [the optimal r_l value found in Fig. 2(c)]. We observe a reduction in Q with increasing resonator width w_0, in good agreement with simulation, which arises due to the increase of lossy torsional energy in the polygon sides with increasing width. Note that the theoretical model does not capture the width dependence of the Q, but agrees well with the data when $w_0 \leq 200$ nm and $r_l < 1$. As expected from FEM simulations, we do not observe a clear dependence of Q on the number of sides (N). The data spread in Figs. 2(c) and Fig. 2(d) is mainly caused by the fabrication imperfections (see Appendix D).

In Fig. 3(a), we survey the measured quality factors of fundamental perimeter modes in resonators with different geometries: $N = 4$, 6, and 8, $r_l = 0.2$, 0.4, 0.6, and 0.8, and $w_0 = 200$ and 300 nm. For each mode, we perform multiple measurements with different duty cycles to rule out optical damping and antidamping effects on the Q (see Appendix H). The presented data span many combinations of r_l, w_0, and N, while the FEM simulations are shown only for the optimum design with $r_l = 0.6$ and $w_0 = 200$ nm. Optimally designed samples that are free of fabrication imperfections show good agreement with the FEM simulations. Simulated Q's of the perimeter modes for the optimum design are lower than the clampless limit by a factor of about 1.5 due to additional distributed torsional energy. Our measurements corroborate that the dissipation dilution of perimeter modes scales with device length according to $D_Q \propto 1/\lambda^2$, which shows that these modes are soft clamped. Our highest measured Q is 3.6×10^9 for a 700 μm square with a fundamental

perimeter mode at 350 kHz with an effective mass of $m_{eff} = 17$ pg (estimated from FEM simulation) and zero-point motion of $x_{ZPF} = \sqrt{\hbar/2m_{eff}\Omega_m} = 37$ fm.

In polygon resonators, the boundary losses are eliminated for a whole family of perimeter modes that have nodes at the tethers. We characterize the Q of the first six harmonics of the perimeter mode for a square with $l_0 = 700$ μm, $w_0 = 200$ nm, and $r_l = 0.2$. As expected from simulations, the harmonics of the perimeter mode also show significantly higher D_Q with respect to the out-of-plane flexural modes of a doubly clamped beam [Fig. 3(b)].

IV. POLYGON RESONATORS WITH A WIDTH CORRUGATION FOR EFFICIENT OPTICAL READOUT

Nanomechanical resonators are commonly interrogated using free-space optical interferometers [41,42]. However, efficient free-space optical readout of high aspect ratio strings is challenging due to their suboptical-wavelength dimensions. To overcome this challenge, we fabricate square-shaped polygon resonators with side segments whose width is increased at the center. The region with increased width forms a pad that reflects more light. The relation between Q and width of the pad involves a combination of stress relaxation, torsional losses, and mode hybridization. We study the width dependence using FEM simulations (see Appendix C) and choose pad widths for which the Q degradation is minor (less than 50%). Figures 4(a) and 4(b) show a dark-field microscope image of a square-shaped resonator with a reflection pad where the width w is increased with a cosine profile over 100 μm.

Figure 4(d) shows the experimental setup used for position measurement of the devices. Light is focused on the resonator using a microscope objective and the reflected light is detected in a balanced homodyne scheme. The mechanical modes appear as sidebands in the homodyne noise spectrum. The power of these sidebands (i.e., area under each one) is proportional to the reflected optical power from the resonator and the amplitude of the mechanical oscillations at the probing point. To study the effect of the width corrugation, we measure the mechanical sideband power of the perimeter mode P_m at different positions on a polygon side. Since the width of the segment ($w_0 = 700$ nm) is comparable to the optical wavelength (768 nm), the reflected power depends on the width at the probing point. In Fig. 4(c) we show P_m at each point on the side segment. As expected, in the regions where the width is constant, P_m follows the mode shape of the perimeter mode. When the laser beam is focused on the pad, we observe an improvement of about 5.5 in P_m compared to the constant width case. To avoid the effects of optical driving, this measurement is done at high
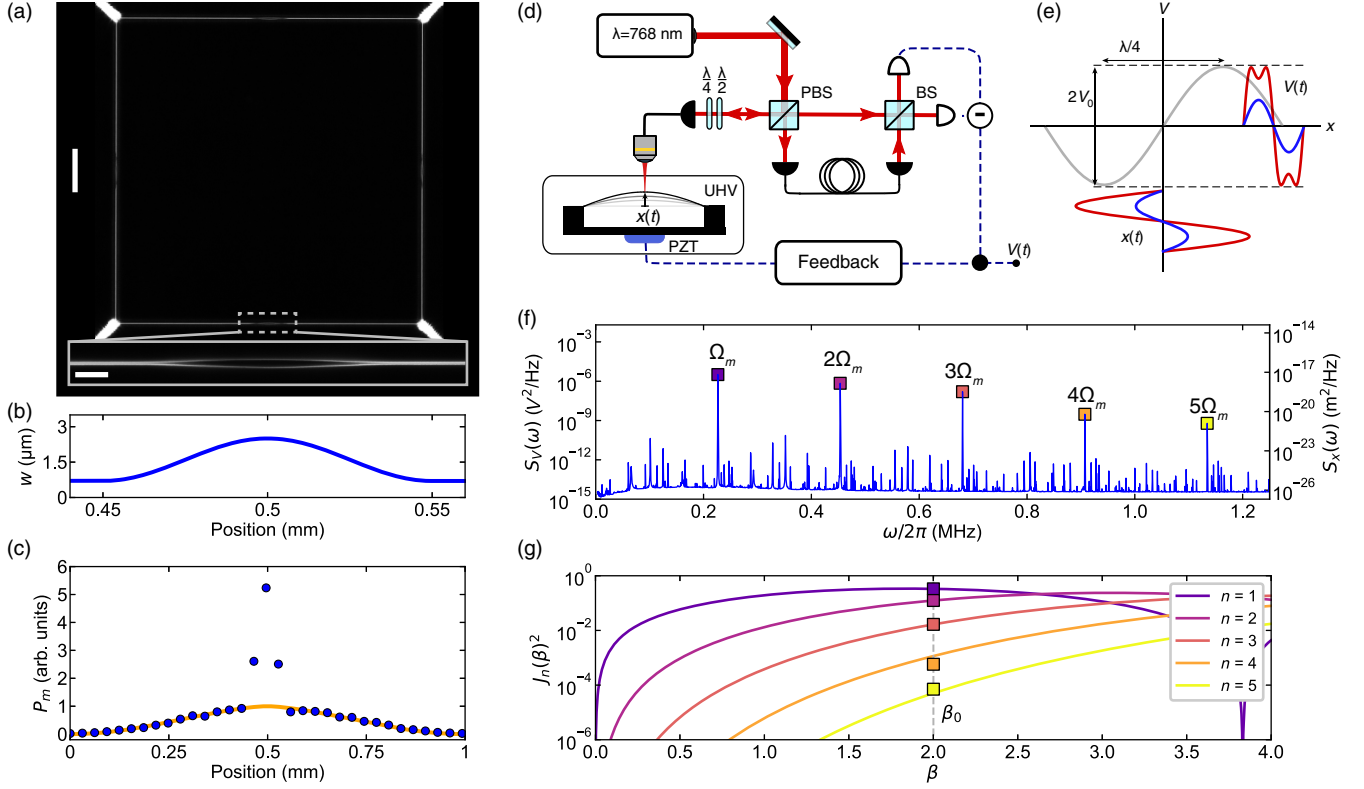
FIG. 4.   Polygon resonators with width corrugations and interferometric readout. (a) Dark-field microscope image of a square-shaped polygon resonator with width corrugations (inset). White scale bars: main image, $100~\mu m$; inset, $10~\mu m$. Device parameters: $l_0 = 700~\mu m$, $r_l = 0.35$, and w_0 increased from 700 nm to $2.5~\mu m$ in the width corrugation. (b) The width profile of the pad shown in the inset of (a). (c) Perimeter mode thermomechanical sideband power at different positions on the side segment of a 1 mm square-shaped polygon resonator with width corrugations similar to the ones shown in (a) and (b). Blue circles: measured sideband power. Orange curve: expectation from the mode shape of the perimeter mode along a side segment (obtained from a FEM simulation). (d) Experimental setup used for interferometric position measurement and feedback control of the resonators. UHV: ultrahigh vacuum chamber with pressure below 10^{-8} mbar. PZT: piezoelectric actuator. Feedback: lock-in amplifier and digital phase-locked loop (PLL) employed to synthesize a feedback signal for the piezoelectric actuator. (e) Working principle of displacement calibration using nonlinear transduction in an interferometer. The gray line shows the transduction curve of the interferometer. The blue and red lines correspond to linear and nonlinear transduction regimes, respectively. (f) PSD of the homodyne signal $S_V(\omega)$ (left) and corresponding calibrated displacement PSD $S_x(\omega)$ (right) for the driven motion of the perimeter mode. Boxes mark sidebands at the higher-order harmonics of the perimeter mode that are created due to the interferometer nonlinearity. (g) Fit of the first five Bessel functions to the five sidebands shown in (f). Gray dashed line corresponds to the fit value for β_0 and boxes correspond to the normalized sideband amplitude $A_n/V_0 q_n(\phi_0)$.

pressure ($\sim 1 \times 10^{-3}$ mbar) where the linewidths of the modes are broadened due to gas damping.

To calibrate the homodyne spectra in terms of displacement, we utilize the nonlinear transduction regime of the interferometer [43]. Consider a mode with frequency Ω_m whose displacement at a fixed probe position is given by $x(t) = x_0 \cos \Omega_m t$. The output voltage of the balanced homodyne is given by $V(t) = V_0 \sin(\phi_0 + \beta_0 \cos \Omega_m t)$, where $\beta_0 = 4\pi x_0/\lambda_L$ and V_0 and ϕ_0 are the fringe amplitude and quadrature angle, respectively, and λ_L is the laser wavelength. For small oscillation amplitudes ($x_0 \ll \lambda_L$), the interferometer linearly transduces the displacement to voltage as $V(t) = Dx(t)$, where $D = (4\pi V_0/\lambda_L) \cos \phi_0$. Knowing V_0, one can utilize the optical wavelength as a ruler for displacement calibration.

However, V_0 cannot be readily determined when there are spurious reflections not originating from the mechanical resonator, for example, from the chip substrate, tens of micrometers below the nanobeam. V_0 can be calibrated by coherently driving the mechanical mode to high oscillation amplitudes. When the amplitude of oscillations approaches $\lambda_L/8$, V_0 can be determined by analyzing the frequency components of the nonlinearly transduced voltage at harmonics of Ω_m [see Fig. 4(e)]. This method is robust to spurious reflections since the nonlinearly transduced signal originates from the mechanical resonator. The single-sided power spectral density (PSD) of $V(t)$, $S_V(\omega)$ (see Appendix I for the definition), features multiple sidebands of the mechanical mode:

$$S_V(\omega) = 2\pi V_0^2 \sum_{n=1}^{\infty} q_n^2(\phi_0) J_n^2(\beta_0) \delta(\omega - n\Omega_m), \quad (4)$$

where $q_n(\phi_0) = \sqrt{1 - (-1)^n \cos 2\phi_0}$, $J_n(\cdot)$ are the Bessel functions of the first kind, and $\delta(\cdot)$ is Dirac's δ function. Note that in reality the sidebands have finite linewidths. In Fig. 4(f) we show $S_V(\omega)$ obtained from a resonator with $l_0 = 1$ mm and pads with dimensions similar to the one shown in Fig. 4(b), for 350 μW of optical power focused on the pad. The perimeter mode at 226 kHz is driven to an amplitude of $x_0 = 122$ nm (determined by the calibration). Sideband amplitudes A_n, defined as the square root of the area under each peak, can be directly computed from the experimental homodyne spectra. From Eq. (4), the sideband amplitudes are given by $A_n = V_0 q_n(\phi_0) J_n(\beta_0)$.

The calibration parameters (V_0, ϕ_0, and β_0) can be obtained by fitting this model to the data [see Figs. 4(f) and 4(g)]. The displacement PSD can then be found as $S_x(\omega) = D^{-2} S_V(\omega)$. The calibrated $S_x(\omega)$, for the spectrum shown in Fig. 4(f), is shown on the right-hand axis. The noise floor, i.e., the imprecision noise in the position measurement, reaches a level of $S_x^{\mathrm{imp}} = 0.9 \times 10^{-26}$ m^2/Hz at 226 kHz, equivalent to displacement fluctuations of 96 fm in a 1 Hz bandwidth. For a mechanical mode with frequency of Ω_m, linewidth of Γ_m, and effective mass of m_{eff}, one can also define a thermal-phonon-equivalent imprecision [3] as $n_{\mathrm{imp}} = S_x^{\mathrm{imp}}/2S_x^{\mathrm{ZPF}}$, where $S_x^{\mathrm{ZPF}} = 2\hbar/m_{\mathrm{eff}}\Omega_m\Gamma_m$ is the peak value of the zero-point fluctuations' PSD. For the 1 mm device mentioned above we measure a quality factor of 1.5×10^9 and compute an effective mass of 101 pg (using a FEM simulation). The thermal-phonon-equivalent imprecision for this device amounts to $n_{\mathrm{imp}} = 0.003$.

V. THERMAL-NOISE-LIMITED FORCE SENSING

Force sensing using mechanical oscillators relies on referring displacement fluctuations of a mode to force fluctuations using the known susceptibility of the mechanical mode [44]. Consider a mechanical mode with resonance frequency Ω_m, linewidth of Γ_m, and effective mass m_{eff}. The frequency response of the displacement of the mode $x(t)$ to a force to be measured $F_{\mathrm{ext}}(t)$ is given by $x(\omega) = \chi_m(\omega) F_{\mathrm{ext}}(t)$, where $\chi_m(\omega)$ is the susceptibility given by

$$\chi_m(\omega) = [m_{\mathrm{eff}}(\Omega_m^2 - \omega^2 - i\Omega_m\Gamma_m)]^{-1}, \quad (5)$$

where we have assumed a structural damping model [45]. In a realistic setting the mechanical mode is in thermal equilibrium at temperature T and is subject to the stochastic thermal force $F_{\mathrm{th}}(t)$. The displacement measurement record $x_{\mathrm{meas}}(t)$ also includes the measurement imprecision, i.e., $x_{\mathrm{meas}}(t) = x(t) + x_{\mathrm{imp}}(t)$. As a result, if the

displacement measurement record has PSD of $S_x^{\mathrm{meas}}(\omega)$, the force-referred noise PSD, $S_F^{\mathrm{meas}}(\omega)$, is given by $S_x^{\mathrm{meas}}(\omega)/|\chi_m(\omega)|^2$, which amounts to

$$S_F^{\mathrm{meas}}(\omega) = S_F^{\mathrm{ext}}(\omega) + S_F^{\mathrm{th}}(\omega) + S_F^{\mathrm{imp}}(\omega), \quad (6)$$

where $S_F^{\mathrm{ext}}(\omega)$ is the PSD of the external force, $S_F^{\mathrm{th}}(\omega) = 4m_{\mathrm{eff}}k_B T\Gamma_m$ is the PSD of the thermal force, and $S_F^{\mathrm{imp}}(\omega) = S_x^{\mathrm{imp}}(\omega)/|\chi_m(\omega)|^2$ is the force-referred measurement imprecision. Evidently, the force sensitivity is limited by the thermal force and the imprecision. Therefore, one can only perform thermal-noise-limited force sensing in a bandwidth determined by the imprecision level. For a thermal-phonon-equivalent imprecision of n_{imp}, the 3 dB bandwidth of thermal-noise-limited force sensing is given by $\Delta\omega_{\mathrm{th}} = \sqrt{(n_{\mathrm{th}}/n_{\mathrm{imp}})}(\Gamma_m/2)$, where $n_{\mathrm{th}} = k_B T/\hbar\Omega_m$ is thermal phonon occupancy of the mode.

Thermal-noise-limited force sensing requires resolving the Brownian motion of the mechanical mode. Our best polygon resonators have linewidths as low as $\Gamma_m = 2\pi \times 100$ μHz. Reaching this level of spectral resolution requires a measurement record of at least 3 hours. However, for such long data acquisitions, the measurement is sabotaged by frequency fluctuations of the mechanical mode, potentially caused by measurement setup alignment drifts, ambient temperature fluctuations, and heating from optical absorption. Nevertheless, one can circumvent these issues by broadening the mechanical linewidth by means of measurement-based feedback (i.e., feedback cooling) [21,46,47]. Introducing a feedback force proportional to the oscillator's delayed displacement, $F_{\mathrm{fb}}(t) = -m_{\mathrm{eff}}\Omega_m^2 g_{\mathrm{fb}} x(t - \tau_{\mathrm{fb}})$, modifies the mode's susceptibility. For a quarter period delay ($\tau_{\mathrm{fb}} = \pi/2\Omega_m$) the effective susceptibility of the mode is

$$\chi_{\mathrm{eff}}(\omega) = [m_{\mathrm{eff}}(\Omega_m^2 - \omega^2 - i\Omega_m\Gamma_{\mathrm{tot}})]^{-1}, \quad (7)$$

where $\Gamma_{\mathrm{tot}} = \Gamma_m(1 + Q g_{\mathrm{fb}})$ is the broadened linewidth. In the classical regime, the linewidth broadening results in cooling to an effective temperature of

$$T_{\mathrm{eff}} = \frac{\Gamma_m}{\Gamma_{\mathrm{tot}}} T. \quad (8)$$

As a consequence, in a force sensing experiment with a feedback cooled oscillator, one will obtain the same thermal-limited force sensitivity and force-referred measurement imprecision as if the oscillator was not feedback cooled (see Appendix J for a detailed derivation). The benefit of using feedback cooling is that the broadened mode has a faster response and the Brownian motion can be fully resolved with much shorter measurement records, thereby alleviating experimental stability requirements [21].
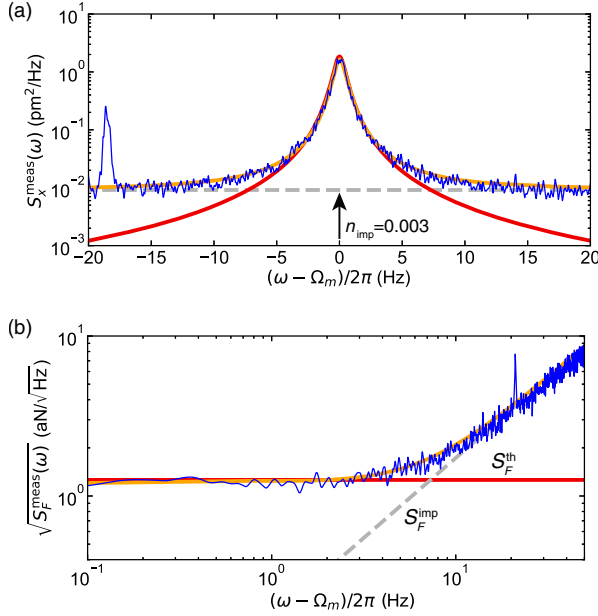
FIG. 5. Feedback cooling and thermal-noise-limited force sensing. (a) Displacement fluctuation PSD of the feedback cooled perimeter mode. Blue line: experimental data. Orange line: Lorentzian fit to the data which gives a total linewidth of $\Gamma_{\text{tot}} = 2\pi \times 1.0$ Hz. Red line: expected Brownian motion PSD. Dashed gray line: the imprecision noise background in the displacement measurement. (b) Force noise PSD. Blue and orange lines are the experimental data and the Lorentzian fit shown in (a), divided by the effective susceptibility [Eq. (7)]. Red line: the expected thermal force PSD. Dashed gray line: contribution from imprecision.

To demonstrate feedback cooling and thermal-limited force sensing, we use the square-shaped resonator with $l_0 = 1$ mm and reflection pads mentioned in the previous section. For applying the feedback force, we use a piezo-electric actuator whose drive frequency is phase locked to the perimeter mode, using the demodulated homodyne signal and a phase-locked-loop module [Fig. 4(d)]. Figure 5(a) shows the PSD of the measured position $S_x^{\text{meas}}(\omega)$. Feedback cooling broadens the mode's linewidth to $\Gamma_{\text{tot}} = 2\pi \times 1.0$ Hz, inferred from a Lorentzian fit. The measured PSD is in good agreement with the expected thermal fluctuation PSD of the broadened mode $[|\chi_{\text{eff}}(\omega)|^2 S_F^{\text{th}}(\omega)]$. For the theoretical model the effective mass is estimated from a FEM simulation and $\Gamma_m = 2\pi \times 151$ μHz is found independently using gated ringdown measurements. Integration of the measured PSD reveals an effective temperature of $T_{\text{eff}} = 44$ mK equivalent to phonon occupation of 4.1×10^3. The force-referred noise PSD is shown in Fig. 5(b), comparing the experimental data with the expectation from Eq. (6) (in the absence of the external force). This analysis reveals a thermal-noise-limited force sensitivity of $\sqrt{S_F^{\text{th}}} = 1.3$ aN/$\sqrt{\text{Hz}}$. The thermal-noise-limited force sensing bandwidth measured from the spectrum in Fig. 5(b) amounts to $\Delta\omega_{\text{th}} = 2\pi \times 7.3$ Hz.

VI. PHONONIC DIMERS AND ARRAYS

Coupled mechanical resonators are used for mass and charge sensing [48,49] and studies of fundamental multimode dynamics [50,51]. The torsional deformations in the tethers can be utilized to couple the perimeter modes of two polygon resonators [Fig. 2(a)]. By joining two square-shaped resonators with a tether, we induce torsional coupling between the perimeter modes [as in the device in Fig. 6(b)]. This coupling results in hybridization of the two perimeter modes of the two resonators into a pair of new modes. As shown in Fig. 6(a), these modes are "in-phase" and "out-of-phase" combinations of the two perimeter modes. Because of the symmetries of these modes, the deformation of the coupler segment takes two different forms. For the in-phase mode, the antisymmetric displacement results in torsional deformation while for the out-of-phase mode the deformation is solely rotational and therefore stores no elastic energy [Fig. 6(a)].

The strength of the coupling (i.e., the hybridized modes' frequency splitting) is determined by the dimensions of the coupler segment [w_c and l_c, shown in the inset of Fig. 6(d)]. Using FEM simulations, we find an approximately linear relation between the frequency splitting δf and the parameter w_c^2/l_c (see Appendix K for more details). We experimentally study "phononic dimers" with side lengths of 100 μm with different coupling parameters w_c^2/l_c and find the expected hybridization of perimeter modes (see Fig. 6).

In Fig. 6(e), we show the scaling of δf with the coupling parameter, that is in agreement with the FEM simulations. For $\delta f < 10$ kHz, the fabrication disorder can be larger than the coupling strength, which prevents hybridization (see Appendix K for details).

The difference in the deformation of the coupling segments also leads to different dissipation rates for the hybridized modes. The extra torsion of the in-phase mode reduces its quality factor compared to the out-of-phase mode [as shown experimentally in Fig. 6(g)]. This is supported by FEM simulations, and while the experimental quality factors of the out-of-phase modes do not attain the predicted values, they do show reduced loss compared to the in-phase modes [Fig. 6(g)].

The simple design of polygons facilitates coupling of several mechanical resonators with varying nearest-neighbor coupling without any additional design change and by simply changing the width of the coupling segments (w_c) in order to study complex coupled mechanical states. As a proof-of-principle experiment, by choosing coupling rates that alternate between intracell and intercell coupling, J and J', one can realize a one-dimensional Su-Schrieffer-Heeger chain [36]. A SSH chain is an example of a one-dimensional chiral Hamiltonian with nontrivial topology, where the coupling strength is alternated between the sites [J and J' in Fig. 6(c)] [52]. Figure 6(c) shows a fabricated array of six square resonators with side length of 100 μm and alternating coupling rates with simulation values of
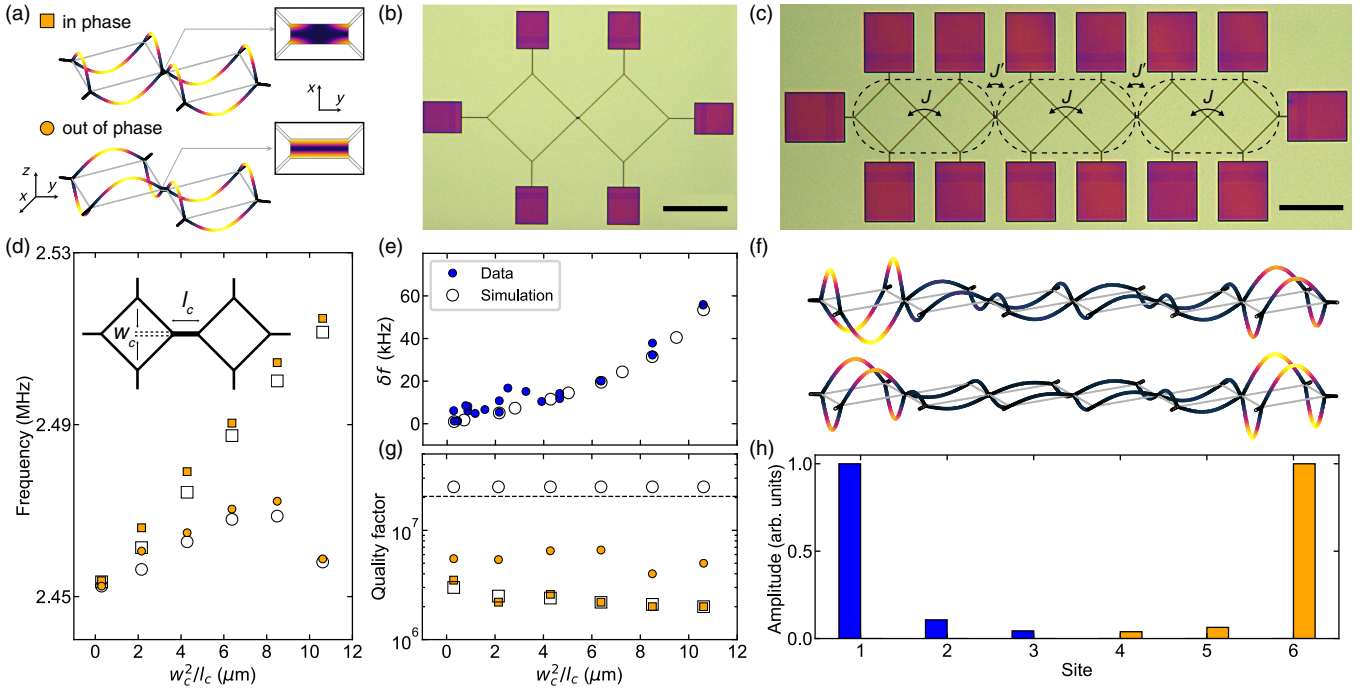
FIG. 6. Phononic dimers and arrays of polygon resonators. (a) FEM simulations of the in-phase and out-of-phase modes of a phononic dimer. The insets show the deformation of the coupler segment for the two cases. (b),(c) Optical micrographs of a fabricated dimer and a chain, both composed of square-shaped resonators with side lengths of 100 μm. The scale bars correspond to 100 μm. (d) The frequencies of the in-phase (square) and out-of-phase (circle markers) modes from data (filled markers) and FEM simulation (empty markers) for different coupling parameters. The inset indicates the coupling parameters of a phononic dimer. (e) Frequency splitting of the in-phase and the out-of-phase modes from data (filled markers) and FEM simulation (empty markers) for different coupling parameters. (f) FEM simulation of the edge mode profiles of a phononic array made of six square-shaped resonators. The slight asymmetry is due to the disorder in the mesh of the simulation. (g) Q of the hybridized modes from data (filled markers) and FEM simulation (empty markers) for different coupling parameters. The dashed line corresponds to quality factor of a single square-shaped resonator. (h) rms values of the Brownian motion of each site measured for the two split modes, showing localization of the mode at the edges of the chain.

$J/2\pi = 0.35$ kHz and $J'/2\pi = 5$ kHz (corresponding to dimer frequency splittings of 0.7 and 10 kHz). In this case, the array can be seen as a three-cell chain of phononic dimers. If the intercell coupling is weaker than the intracell coupling ($J' > J$), the array exhibits edge modes of the perimeter modes of the chain. Figure 6(f) shows FEM simulations of such a mode of this array. This is a collective mode where all the resonators are oscillating in their perimeter mode while the amplitudes of the modes at the "edge" sites of the array are much greater than for the "bulk" sites. However, in practice, fabrication disorder can lift the degeneracy and the two new modes which emerge are not fully symmetric but nevertheless show some edge mode characteristics. We observe two such modes in our structure and characterize them by measuring the rms values of the thermal fluctuations of each mode at each site and observe that both modes are fully localized at one of the edge sites [see Fig. 6(h)]. In an alternative scenario where $J' < J$, the system transitions into a so-called "trivial" phase where the edge modes' degeneracy is fully lifted and their edge characteristics completely vanish. We fabricate an array with flipped order of strong-weak

coupling rates ($J/2\pi = 5$ kHz and $J'/2\pi = 0.35$ kHz) and follow the same measurement procedure. We identify six modes that have frequencies close to that of a single perimeter mode but we do not observe any edge structure in any of them (see Appendix L for the complete mode spectrum). This provides further evidence for topological symmetries playing a significant role in the eigenmodes of our arrays. We measure $Q \approx 10^7$ for the edge modes of the SSH chain which is 50% below the simulation. The simulated Q for the edge modes is equal to the single cell perimeter mode Q, showing that the chains of polygon resonators are capable of retaining the single polygon quality factors. The origin of this discrepancy requires further investigation and could be due to mode hybridization arising from fabrication imperfections (see Appendix D).

VII. CONCLUSION

We demonstrated perimeter modes in vertex-clamped polygon resonators that implement soft clamping without a phononic band gap. Our devices have Q's as high as

3.6×10^9 at room temperature, exceeding the state-of-the-art Q by a factor of 4 with 10 times smaller devices [15]. The enhanced dissipation dilution (D_Q) of the polygons combined with crystalline materials [53,54] could enable Q's exceeding 10^{10} in cryogenic environments. Our highest Q resonator has a thermal-noise-limited force sensitivity of $\sqrt{S_F^{th}} = \sqrt{4k_B Tm\Gamma_m} \approx 420$ zN/$\sqrt{Hz}$ at room temperature, on par with atomic force microscopy cantilevers at milli-kelvin temperatures (190 zN/$\sqrt{Hz}$) [55]. Polygon resonators are well suited for integration in sensing platforms, such as inverted microscope systems, as the multiple sides of the polygon facilitate addition of several probes or measurement specimens on the same mechanical resonator [28,56–58]. One could even imagine functionalizing one side of the polygon by the deposition of a magnetic or metallic coating to provide sensitivity to electric or magnetic fields that could then be read out optically on a different polygon side. With an eye toward sensing applications, we show that by increasing the width of a part of the polygon resonator, we can perform thermal-noise-limited force sensing with a simple free-space interferometer. Efficient interferometric readout of such low dissipation mechanical resonators could also allow cavity-free feedback cooling of the mechanical motion to the quantum ground state [44,59,60].

Near-field coupling allows high optomechanical coupling rates ($g_0/2\pi > 20$ kHz) [3,20,21], but is technically challenging with millimeter-scale structures due to the small gaps required (∼100 nm) between the optical cavity and mechanical resonator. The compact form factor of polygon resonators promises increased mechanical quality factors for integrated optomechanical systems, facilitating room temperature quantum optomechanical experiments such as feedback cooling [2,3], ponderomotive squeezing [61–64], and observation of radiation pressure shot noise [65,66]. Previous demonstrations of integrated optomechanical systems using Si₃N₄ nanobeams [3,19,67,68] have been limited by low mechanical Q and $Q \times f$. A doubly clamped nanobeam with 420 μm length results in $Q = 6 \times 10^6$ and $Q \times f = 3.5 \times 10^{12}$ Hz, which prohibits ground state cooling at room temperature [6]. A polygon with equal clamp-to-clamp length, thickness, and width profile would exhibit $Q = 420 \times 10^6$ and $Q \times f = 3.6 \times 10^{14}$ Hz, resulting in an order of magnitude higher single photon cooperativity (see Appendix N for details) and providing access to the quantum back-action-dominated regime at room temperature.

Finally, we show coupling of polygon resonators forming phononic dimers with controllable mechanical mode splitting which allows us to explore coupled high-Q phononic arrays. Moreover, the coupled polygons provide an alternative platform for parametric spin sensing [27–29] and study of topological states in nanomechanics [69] owing to their controllable mechanical coupling rates and potential for extremely low dissipation.

The supporting data and data analysis codes are available at Ref. [68].

APPENDIX A: THEORY MODEL FOR DISSIPATION DILUTION OF THE PERIMETER MODES

To analytically estimate the dilution factor of perimeter modes, we proceed as in Refs. [10,70]. We express a lossless "tension" energy:

$$\langle W_{tens} \rangle = N\sigma w_0 h \int_0^{l_0} [u'(x)]^2 dx, \qquad (A1)$$

from the out-of-plane displacement profile $u(x)$ along the polygon sides. Here, N is the number of sides, σ is the static stress after relaxation, w_0 is the polygon width, l_0 the side length, and h the film thickness.

The lossy energy is approximated as arising only from bending in the polygon sides and from the torsion of the supporting tethers [70]. Explicitly,

$$\langle W_{bend} \rangle = \frac{NEw_0 h^3}{12} \int_0^{l_0} [u''(x)]^2 dx, \qquad (A2)$$

with Young's modulus E and the integral running over the polygon side, and

$$\langle W_{tors} \rangle = \frac{NEw_s h^3}{6(1+\nu)} \int_0^{l_s} [\tau'(x)]^2 dx, \qquad (A3)$$

with τ torsion angle, evaluated over the supporting tether of length l_s and width w_s. Note that we are neglecting torsion in the polygon side beams, which can contribute significantly for larger side widths.

In order to evaluate the integrals, we assume simplified displacement and torsion profiles. In the polygon sides, the out-of-plane displacement will be almost perfectly sinusoidal for $\lambda \ll 1$, with nodes at the polygon vertices: $u(x) = u_0 \sin(n\pi x/l_0)$ (n is the perimeter mode index). The torsion angle is assumed to decay linearly toward the clamping points [70]. This approximation is acceptable when the support tether length is much smaller than the torsional wavelength at the mechanical frequency of the perimeter

mode. Torsion and out-of-plane displacement are connected by continuity of the displacement field at the joint:

$$\tau(l_s) = \frac{u'(0)}{\sin(\theta)} = \frac{n\pi u_0}{l_0 \cos(\pi/N)}, \tag{A4}$$

where $\theta = \pi/2 - \pi/N$ is the semiangle subtended by two polygon sides.

Since $D_Q = \langle W_{\text{tens}} \rangle / (\langle W_{\text{bend}} \rangle + \langle W_{\text{tors}} \rangle)$, we can distinguish two separate contributions:

$$D_{Q,\text{bend}} = \frac{1}{n^2 \pi^2 \lambda^2}, \tag{A5}$$

$$D_{Q,\text{tors}} = \frac{r_l(1+\nu)\cos^2(\pi/N)}{4(r_w)\lambda^2}, \tag{A6}$$
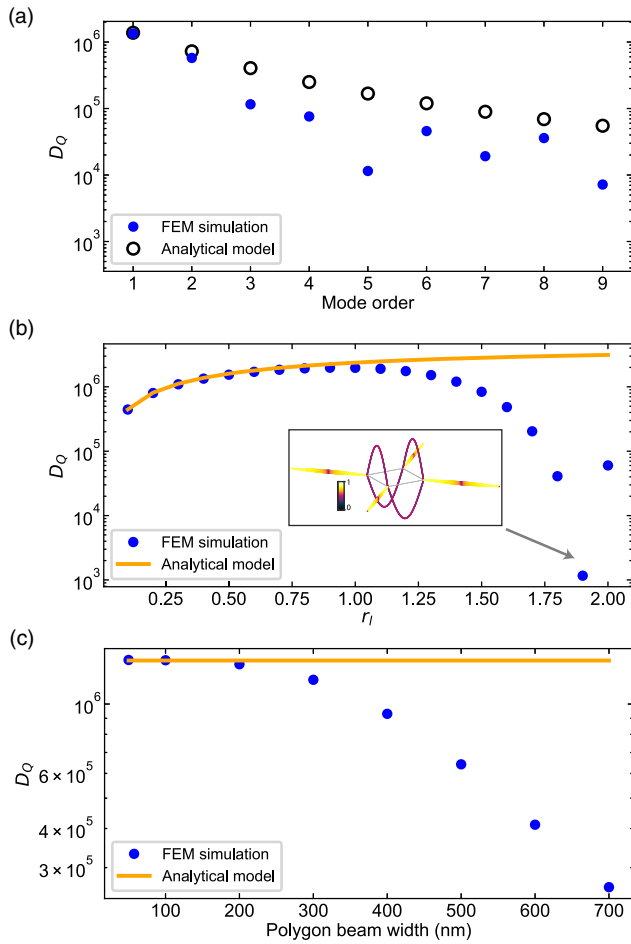

(a)

(b)

(c)

FIG. 7. Theory model and FEM simulation comparison. We compare simulation and analytical predictions for a polygon resonator with $N = 4$, $l_0 = 700 \ \mu m$, and uniform stress ($r_w = \sqrt{2}$). (a) Dilution factor (D_Q) for different perimeter modes ($w_0 = 200$ nm, $r_l = 0.4$). (b) D_Q of the first perimeter mode as the support length is varied (fixed $w_0 = 200$ nm). The inset shows the mode displacement for $r = 1.9$, with the color encoding the torsional energy density. (c) D_Q of the first perimeter mode as the width of all the segments is varied (fixed $r_l = 0.4$).

such that $D_Q^{-1} = D_{Q,\text{bend}}^{-1} + D_{Q,\text{tors}}^{-1}$. Here, we defined $r_l = l_s/l_0$, $r_w = w_s/w_0$, and $\lambda = \sqrt{E/(12\sigma)}h/l$.

The static stress in the polygon segments σ can be found by imposing force balance and conservation of the length of the path separating two polygon clamping points, upon structure release:

$$\sigma = \frac{\sigma_0(1-\nu)[1 + 2r_l \sin(\pi/N)]}{1 + 4(r_l/r_w)\sin^2(\pi/N)}, \tag{A7}$$

where σ_0 is the thin film deposition stress, prior to structure undercut.

Our model provides a good approximation of the D_Q of the first perimeter mode, but in general overestimates it, as evident from the comparison with FEM simulations (Fig. 7). This is mainly due to the simplified assumption that lossy elastic energy is only stored in tether torsion and polygon segments out-of-plane bending, which is valid in the limit where $w/l \to 0$. In the real displacement patterns, the torsion in the polygon segments is also significant, and becomes dominant as the segments get wider [see Fig. 7(c)]. Moreover, the model is less accurate for increasing mechanical frequency and tether length, as the torsion angle profile in the tethers can no longer be approximated as linear [see Figs. 7(a) and 7(b)]. In Fig. 7(b), a minimum of D_Q is observed as the first perimeter mode hybridizes with a tether torsional mode, around $r \approx 1.9$. As a broad criterion, the analytical expression is accurate for the first perimeter mode, and $r_l \leq 0.6$, $w_0 \leq 200$ nm.

APPENDIX B: STRAIN ENGINEERED POLYGON RESONATORS

Dissipation dilution suggests that one method to improve the Q of a soft-clamped mode is to enhance the local stress in the region where the mode is localized [15]. This method—strain engineering—has shown Q enhancement in nanobeam resonators beyond the soft-clamping limit by width tapering the nanobeam to increase the stress in the localized mode region. We investigate strain engineering in polygon resonators in simulations. By keeping the support width (w_s) constant and narrowing the polygon side width (w_0) by a tapering constant $\alpha < 1$, we can enhance the local stress in the sides of the polygon. For a suspended thin film with a fixed deposition stress, the total tension force at the junction is constant, and by narrowing the sides of the polygon stress is enhanced [Eq. (A7)]. We simulate the Q of the strain engineered design shown in Fig. 8(b)(i) (Q_{stress}) and compare it to the stress-preserving design (Q_{normal}) that is studied in this work [Fig. 8(b)(ii)]. We simulate a square with $l_0 = 250 \ \mu m$, $r = 0.6$, $w_0 = 200$ nm, and 20 nm thickness. The simulation results in Fig. 8(a) show possible Q enhancements up to 1.8 times higher than the stress-preserving design.
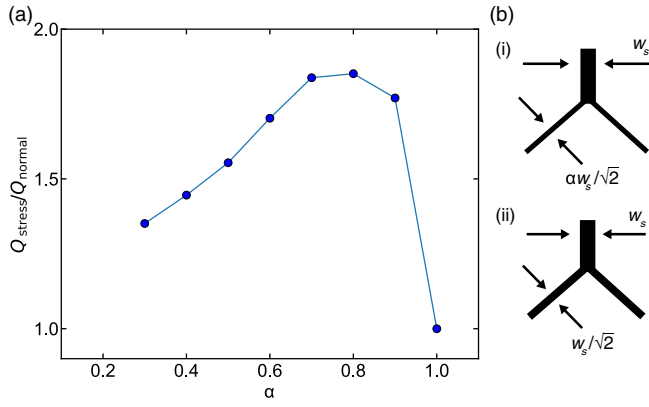
FIG. 8.   Strain engineered polygon resonators. (a) Simulated Q enhancement of polygon resonators via strain engineering (Q_{stress}) compared to the stress-preserving design (Q_{normal}). (b) Schematic of the polygon width tapering for strain engineering (i) and stress-preserved design (ii) for a square-shaped polygon.

FIG. 10.   Fabrication process flow. (1) LPCVD thin film deposition of Si_3N_4 on Si (red on gray). (2) ebeam lithography on Si_3N_4 wafer using FOX16 (blue). (3) Dry etching of Si_3N_4. (4) Recess ebeam (green corresponds to the second layer of FOX16). (5) DRIE etching of Si substrate. (6) KOH undercut and CPD.

APPENDIX C: EFFECT OF THE SIZE OF THE WIDTH CORRUGATION ON Q

For polygon resonators with width corrugations, we use FEM simulations to determine the dependence of the perimeter modes' parameters on the size of the pad. We simulate square-shaped resonators with $l_0 = 1$ mm, $r_l = 0.35$, and two values of w_0. The corrugation has a cosine-shaped width profile [Fig. 4(b)] over $100\ \mu$m. We vary the pad width and calculate frequency, quality factor, effective mass, and S_F^{th} for the perimeter mode. The results
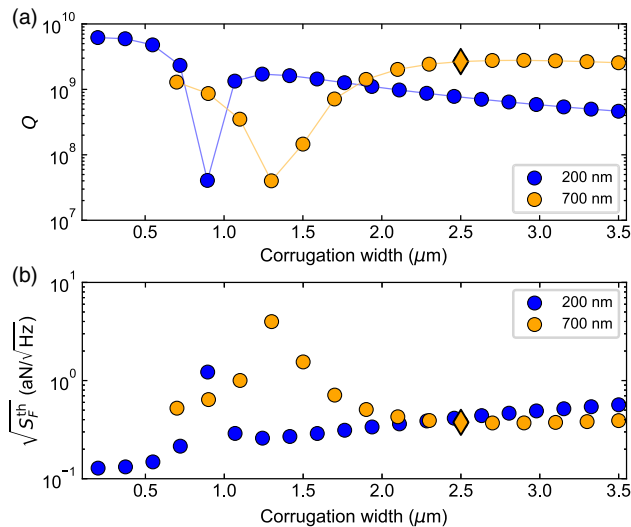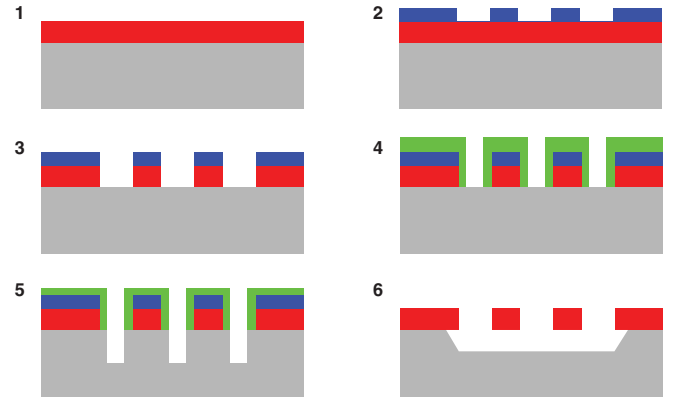
of these simulations are shown in Figs. 9(a) and 9(b). This behavior is due to hybridization of the perimeter mode with the torsional mode in the side segment which results in reduced Q. The optimal pad size must be chosen by considering the conflicting requirements of small effective mass, absence of buckling instabilities, and high mechanical Q.

APPENDIX D: FABRICATION PROCESS FLOW

We fabricate all the samples using 20-nm-thick LPCVD Si_3N_4 on Si wafers. The fabrication process is outlined in Fig. 10. Structures are defined using electron beam (ebeam) lithography using FOX16 resist. During this step, we observe lithography stitching errors due to imperfections in the overlap of the exposure fields of the ebeam process (see Fig. 11). This could be a source of fabrication imperfections. Patterns are transferred into the Si_3N_4 using SF_6-based dry etching. A biased mask is written using the same ebeam lithography process and used for deep reactive

FIG. 9.   Dependence of Q and S_F^{th} on the corrugation width. Square-shaped polygon resonators with corrugated widths are simulated. Q and S_F^{th} are shown in (a) and (b) for $w_0 = 0.2\ \mu$m (blue) and $w_0 = 0.7\ \mu$m (orange). The diamond marker corresponds to the device used in the force sensitivity experiment.
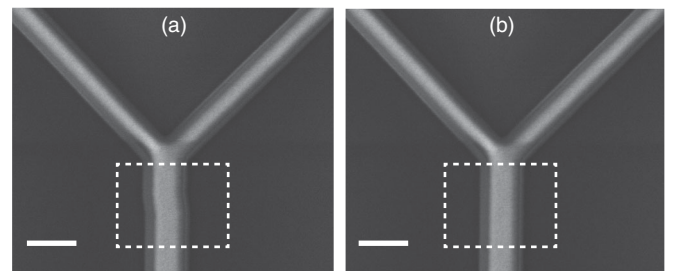

FIG. 11.   ebeam lithography stitching errors. An example of a device with (a) and without (b) stitching errors after the ebeam lithography process. The area of stitching is marked with the white dashed square for comparison. Scale bars correspond to 500 nm.

ion etching (DRIE) of the silicon substrate to create a recess for the final suspension etch. Samples are then diced to chips and cleaned using piranha and BHF solutions prior to the final etch. Si_3N_4 structures are released using KOH wet etching and dried using a critical point dryer (CPD). Full details of the nanofabrication process are available on the NanoFab fabrication archive [39].

APPENDIX E: MODE SPECTRUM OF POLYGON RESONATORS

By measuring the broadband thermomechanical noise spectrum of a polygon resonator, we can label the modes using the frequencies predicted by the FEM simulations. The spectrum shown in Fig. 12(a) is obtained from the device used in Sec. V by focusing the laser beam on the pad. For this measurement, the pressure in the vacuum chamber was increased to 1×10^{-3} mbar to provide substantial gas damping and prevent mode instability. A few of the identified modes are shown in Fig. 12(a) alongside their displacement mode profile. In the FEM simulation, the stress is chosen such that the frequency of the fundamental mode matches the experimentally found frequency. By this anchoring, we find the frequencies of the out-of-plane modes with less than 1% discrepancy, up to the third-order perimeter mode.
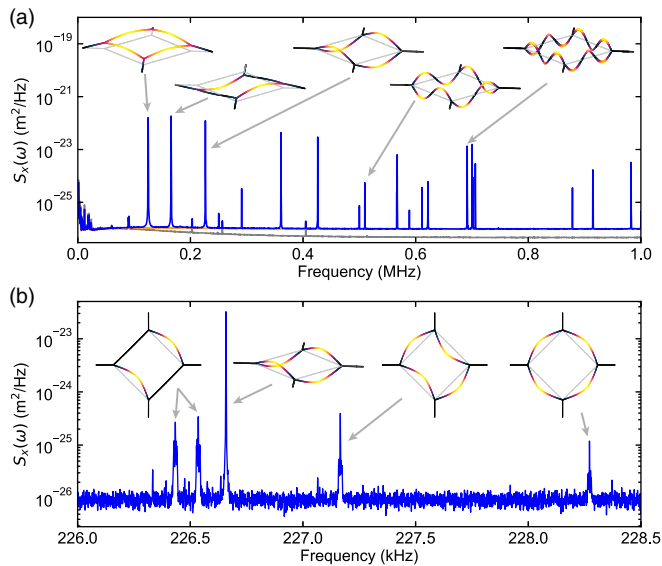

FIG. 12. Mode spectrum of polygon resonators. (a) Blue line: broadband thermomechanical noise spectrum, obtained from the device used in Sec. V. Some of the identified modes are marked with their corresponding mode profile obtained from a FEM simulation. Orange line: signal with only local oscillator light. Gray line: signal with no light incident on detector. (b) Narrowband displacement spectrum around the perimeter mode of the same device; obtained while applying moderate dissipative feedback. The out-of-plane and in-plane perimeter modes are marked.

According to the FEM simulation, in addition to the high-Q out-of-plane mode, there exist four other in-plane modes that are also localized on the perimeter of the polygon (i.e., no displacement in the tethers). Even though the free-space interferometer is weakly sensitive to the in-plane modes, we detect the in-plane perimeter modes in a narrowband spectrum, around the out-of-plane perimeter mode [Fig. 12(b)]. We acquire this spectrum while applying a moderate dissipative feedback at low pressure to avoid mode instabilities. We identify these modes by comparing their frequencies to the prediction from the simulation. The first two in-plane modes are not consistent with the simulation results. This is likely because of hybridization due to fabrication imperfections, as in the simulation the two modes are degenerate.

APPENDIX F: EFFECT OF CHIP MOUNTING ON THE Q

The quality factors of nanomechanical resonators generally experience degradation (clamping losses) when the chip on which they are fabricated is fixed by the application of a force [38,40]. To investigate this degradation, we first leave the chip unclamped on the characterization holder, then clamp the chip tightly using metallic clamps pressing on the edges of the chip and fixed with screws, and measure the quality factor in both cases. We characterize polygons with $l_0 = 150$ μm, $r_l = 0.6$, and $w_0 = 300$ nm, and compare the measured Q. We measure four different devices and observe 1%–10% degradation in the Q for the fixed frame case. Error bars in Fig. 13 show the standard deviation of 4 measurements for each sample. These measurements show that the degradation due to chip clamping conditions are substantially suppressed, as previous studies with unpatterned nanobeams and membranes show substantially larger degradation [38,40].
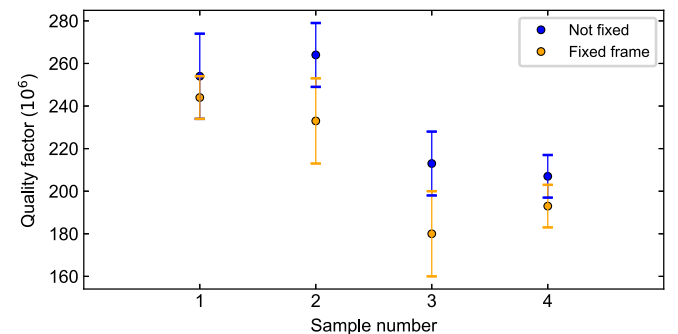

FIG. 13. Effect of chip mounting on the quality factor. Blue dots show the average measured Q when the chip is freely mounted on the sample holder and orange dots correspond to the average measured Q when fixing the chip tightly using metallic clamps pressing on the frame. Error bars show the standard deviation of four measurements for each sample.

APPENDIX G: FREQUENCY STABILITY OF FABRICATED MECHANICAL RESONATORS

For many sensing applications, the frequency stability is a relevant figure of merit. Therefore, we measured the frequency stability of these mechanical resonators by characterizing their Allan deviation. The Allan deviation can be derived in terms of the frequency noise spectrum S_{Ω_m} [71],

$$
\begin{aligned}
\sigma^2(\tau) &= \frac{1}{2\Omega_m^2}\frac{1}{N-1}\sum_{k=2}^{N}(\bar{f}_k - \bar{f}_{k-1})^2 \\
&= \frac{2}{\pi}\left(\frac{2}{\Omega_m\tau}\right)^2\int_{-\infty}^{\infty}d\omega S_{\Omega_m}[\omega]\sin^4(\omega\tau/2)/\omega^2 \\
&= \frac{2}{\pi}\left(\frac{2}{\Omega_m\tau}\right)^2\int_{-\infty}^{\infty}d\omega S_{\phi}[\omega]\sin^4(\omega\tau/2),
\end{aligned}
\tag{G1}
$$

where $\overline{f}_k$ is the averaged frequency of the oscillator over the kth measurement fragment of duration τ, and the relation $S_{\Omega_m}[\omega] = \omega^2 S_\phi[\omega]$ is used.

The thermomechanical phase noise of the oscillator in the strong drive limit is given by

$$
S_\phi[\omega] = \frac{1}{\langle X_{\text{osc}}^2\rangle}\frac{k_B T}{m\Omega_m^2}\frac{\Gamma/2}{\omega^2 + (\Gamma/2)^2} = \frac{\langle X_{\text{th}}^2\rangle}{\langle X_{\text{osc}}^2\rangle}\frac{\Gamma/2}{\omega^2 + (\Gamma/2)^2};
\tag{G2}
$$

therefore, the Allan deviation can be simplified to

$$
\sigma^2(\tau) = \frac{\langle X_{\text{th}}^2\rangle}{\langle X_{\text{osc}}^2\rangle}\frac{1}{Q_m\Omega_m\tau}\frac{(\tau\Gamma_m)^2}{1 + (\tau\Gamma_m)^2}.
\tag{G3}
$$

The other noise sources are the detection noise and the long time linear drift. The detection noise $S_\phi^d(\omega) = [(\Delta f S_{\text{noise}})/\langle X_{\text{osc}}^2\rangle]\{(\Delta f/2)/[\omega^2 + (\Delta f/2)^2]\}$ is assumed to arise from a flat background noise S_{noise} in the measurement record, limited only by the detection bandwidth Δf. When τ is much longer than the detection time $(\sim 1/\Delta f)$, the Allan deviation caused by the detection noise is $\sigma_d(\tau) = \sqrt{[(\Delta f S_{\text{noise}})/\langle X_{\text{osc}}^2\rangle][(2\pi\Delta f)/\Omega_m^2\tau]}$. For the long time linear drift $\delta\Omega_m/\Omega_m = Dt$, the Allan deviation is $\sigma_l(\tau) = [(D\tau)/\sqrt{2}]$.

To investigate the frequency stability of our resonators, we use a phase-locked loop (PLL) with a bandwidth of 1 kHz to track the mechanical frequency fluctuations in our optical interferometer. The measurement result is shown in Fig. 14. The result indicates that the mechanical frequency stability is limited by the linear drift (rate $D \sim 10^{-8}$ s^{-1}) at long τ limit, which masks the extremely low thermomechanical noise-induced frequency fluctuations (Fig. 14), many orders of magnitude below. The rate
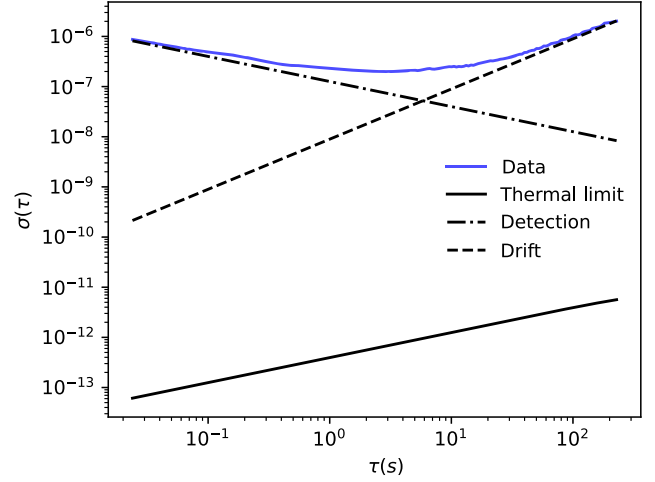

FIG. 14. Frequency stability of perimeter modes. The measurement result of Allan deviation of a 1 mm square-shaped sample with $w_0 = 200$ nm and $r_l = 0.2$ is plotted in blue dots. The dash-dotted line shows the calculated detection limit based on the measurement SNR, and the dashed line is the fit to the linear frequency drift in the long time limit. The fit yields a drift rate $D \sim 10^{-8}$ s^{-1}, which varies among different samples. The theoretical thermal mechanical limit is plotted in black line, which is many orders of magnitude below the measured Allan deviation, due to the exceptionally high quality factor. The scaling is reversed from the usual $\tau^{-1/2}$ to $\tau^{1/2}$ because we are in the limit where the mechanics lifetime is longer than the measurement time $\tau < 1/\Gamma_m$.

of this linear drift varies between different samples and is consistent with the long-term drift in the resonance frequency observed over 24 hours. As the frequency drift is always positive (i.e., increases the resonance frequency), it could be caused by mass reduction due to evaporation of a volatile contaminant on the resonator inside the vacuum chamber.

APPENDIX H: OPTICAL ANTIDAMPING IN RINGDOWN MEASUREMENTS

We investigate the effect of the optical laser beam on the measured mechanical Q to eliminate any effect of optical damping or antidamping [15]. Figure 15 shows that the optical antidamping can be comparable to the damping rate of the oscillator when the measurement laser is left on during the ringdown. We then perform stroboscopic ringdown measurements where we open a laser shutter for 1 s and vary the time in which the measurement laser is off. By varying the duty cycle ($= [t_{\text{on}}/(t_{\text{on}} + t_{\text{off}})]$) we observe that the effect of the measurement laser is negligible for long duty cycles. For the Q's reported in this work, we verify that the Q does not change when varying the duty cycle by a factor ranging from 4 to 10. The reported Q's are an average value of at least four individual ringdowns with the same duty cycle.
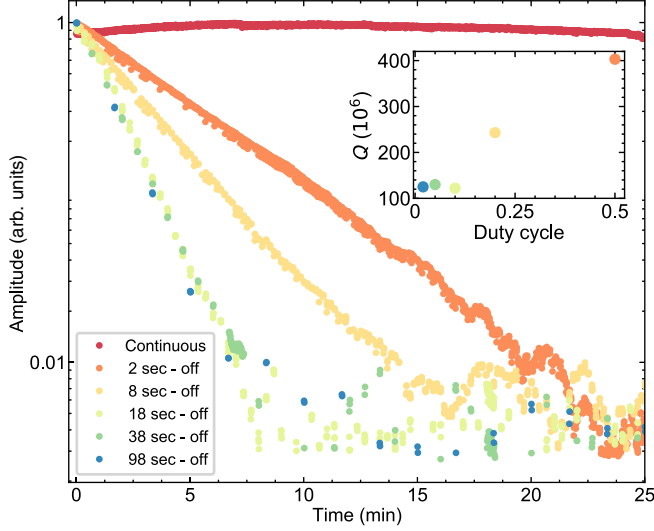
FIG. 15.   Measurement of laser antidamping for different duty cycles. Ringdown measurement of a polygon resonator with varying duty cycles of the measurement strobes. The laser off time is swept while the on time is fixed to 1 s. Q's are calculated from exponential fits to the data and are shown in the inset with marker color corresponding to the data traces.

APPENDIX I: DEFINITION OF POWER SPECTRAL DENSITIES

For a quantity $y(t)$, the double-sided power spectral density is defined as

$$S_{yy}(\omega) = \int_{-\infty}^{\infty} \langle y(t)y(t+\tau)\rangle e^{-i\omega\tau}d\tau, \qquad (I1)$$

where the average $\langle \cdot \rangle$ is an ensemble average for stochastic quantities [e.g., $x(t)$] and a temporal average for periodic signals [e.g., $V(t)$ in Sec. IV]. For stochastic signals, the PSD is simply given by $S_{yy}(\omega) = \langle |y(\omega)|^2 \rangle$. However, measured spectra are in fact the single-sided power spectral densities defined as

$$S_y(\omega) = \begin{cases} 0 & \omega < 0 \\ 2S_{yy}(\omega) & \omega > 0. \end{cases} \qquad (I2)$$

APPENDIX J: MATHEMATICAL DETAILS OF FORCE SENSING IN THE PRESENCE OF FEEDBACK COOLING

In the absence of an external force F_{ext}, the equation of motion for the mechanical mode in the frequency domain is given by

$$\chi_m^{-1}(\omega)x(\omega) = F_{th}(\omega) + F_{fb}(\omega). \qquad (J1)$$

The feedback force is proportional to the delayed measured displacement, $x_{meas}(t - \tau_{fb})$, where for a moderately high-Q mode in the frequency domain it amounts to

$$F_{fb}(\omega) = m_{eff}\Omega_m^2 g_{fb}e^{i\phi_{fb}}[x(\omega) + x_{imp}(\omega)]. \qquad (J2)$$

The solution of Eq. (J1) for this feedback force is given by

$$x(\omega) = \chi_{eff}[F_{th}(\omega) + m_{eff}\Omega_m^2 g_{fb}e^{i\phi_{fb}}x_{imp}(\omega)]. \qquad (J3)$$

Using the definitions given in Appendix I one can find the PSDs for x and x_{meas}:

$$S_x(\omega) = |\chi_{eff}(\omega)|^2[S_F^{th}(\omega) + m_{eff}^2\Omega_m^4 g_{fb}^2 S_x^{imp}(\omega)], \qquad (J4)$$

$$S_x^{meas}(\omega) = |\chi_{eff}(\omega)|^2[S_F^{th}(\omega) + |\chi_m(\omega)|^{-2}S_x^{imp}(\omega)]. \qquad (J5)$$

To find the measured force noise PSD, $S_F^{meas}(\omega)$, we divide $S_x^{meas}(\omega)$ by $|\chi_{eff}(\omega)|^2$ and the result is the one given in Eq. (6). In short, the trace of feedback in $S_F^{meas}(\omega)$ disappears due to the interference between $x(\omega)$ and $x_{imp}(\omega)$ and division by the effective susceptibility.

APPENDIX K: SIMULATIONS OF THE PHONONIC DIMERS

We simulate the mode splitting of the dimers for squares of 150 μm side length, 300 nm side width, and $r = 0.2$. We sweep the length of the coupler for different coupler widths as shown in Fig. 16(a). We find that the
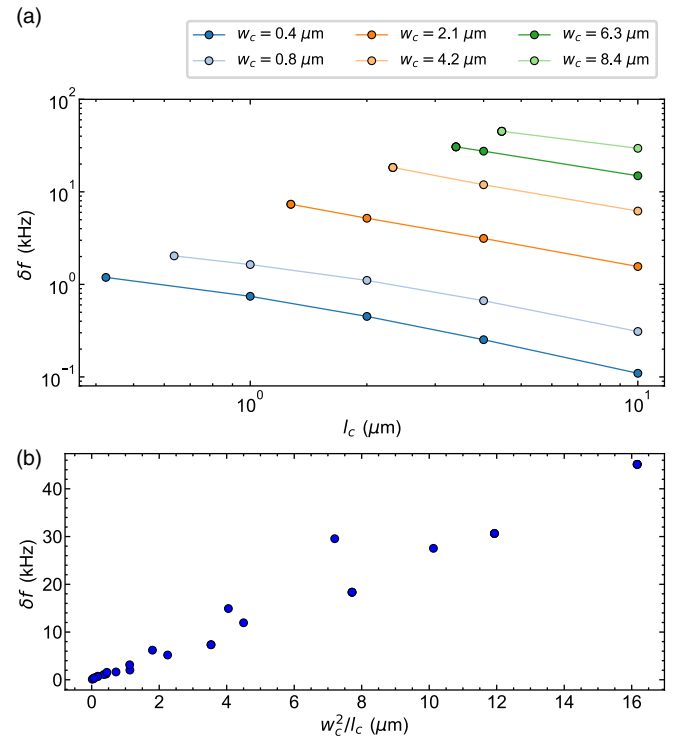

FIG. 16.   Frequency splitting of dimers. (a) FEM simulation of mode splitting for varying coupler length (l_c) and different coupler widths (w_c). (b) Compilation of all the simulated values in (a) plotted versus w_c^2/l_c.

mode splitting depends approximately linearly on w_c^2/l_c, where w_c is the width of the coupling segment and l_c is the length of the coupling segment [Fig. 16(b)]. Since the coupler width dependence of the mode splitting is stronger than the length dependence, we choose the shortest and widest possible couplers to overcome the disorder in the dimers and chains. The minimum coupler length for a given width is determined by the requirement that the coupler segment must be attached on all four corners. Therefore, for wider couplers compared to the beam width, we adapt the coupler length such as to avoid buckling and deformation of the coupling segment after device suspension.

APPENDIX L: FULL MODE SPECTRA OF THE PHONONIC ARRAYS

A chain of n polygon resonators has many flexural modes and we only consider the perimeter modes of the structure. We identify n perimeter modes of the chain by excluding modes with nonzero amplitude on the supporting tethers. Using the same approach as explained in the main text, we find the mode profiles of the collective perimeter modes in the spectrum of both topological and trivial chains. These modes have frequencies in the proximity of the perimeter mode of a single site and have no amplitude on the tethers (verifying that they are localized on the perimeters). These mode profiles are shown in Fig. 17. One can observe that the edge modes are only present in the topological case. Nevertheless, the profile of the other modes as well as the order of their appearance in the spectrum are dominated by the disorder in the fabricated devices.
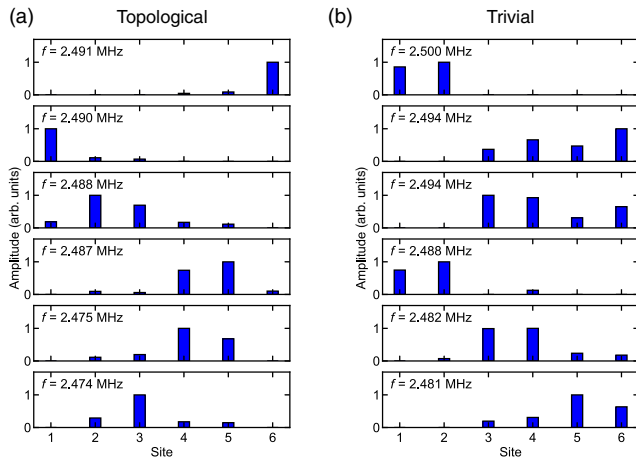

FIG. 17. Mode profiles of the collective perimeter modes. rms values of the Brownian motion of each site measured for all the collective perimeter modes of both topological (a) and trivial (b) chains of six square-shaped resonators.

APPENDIX M: DISORDER IN PHONONIC DIMERS AND ARRAYS

Fabrication imperfections cause dimer and array devices to deviate from an ideal model of coupled identical resonators. These deviations manifest as asymmetry in the hybridized modes of dimers or loss of topological protection in arrays. In reality the disorder can be the result of various processes (e.g., inhomogeneous stress distribution or imperfections in the lithography step). However, one can reduce all the imperfections to a difference between the bare frequencies of the resonators and characterize the disorder using a simple model of coupled harmonic oscillators. In particular, for an "imperfect" dimer, the Hamiltonian can be written in the frame rotating with the average frequency of the two resonators as

$$H = \begin{pmatrix} \delta & J \\ J & -\delta \end{pmatrix}, \qquad (M1)$$

where J is the coupling rate and δ is the absolute value of half of the difference between the bare frequencies. The eigenfrequencies of this Hamiltonian are given by $\omega_\pm = \pm\sqrt{\delta^2 + J^2}$ corresponding to eigenvectors

$$V_+ = \begin{pmatrix} J \\ \sqrt{J^2 + \delta^2} - \delta \end{pmatrix}, \qquad (M2)$$

$$V_- = \begin{pmatrix} \sqrt{J^2 + \delta^2} - \delta \\ -J \end{pmatrix}, \qquad (M3)$$

where $+$ and $-$ correspond to in-phase and out-of-phase modes, respectively. Here we observe that the disorder parameter δ not only contributes to the frequency splitting, but also results in an asymmetry between the amplitudes of perimeter modes of each resonator in the hybridized modes. In our experiment, this asymmetry manifests as a difference between the detected SNR of the hybridized modes when the interferometer is focused on sides of the two resonators [Figs. 18(a) and 18(b)]. According to Eqs. (M2) and (M3), the ratio of the smaller amplitude to the larger one is given by

$$R = \sqrt{1 + \frac{\delta^2}{J^2}} - \frac{\delta}{J}. \qquad (M4)$$

We measure this ratio by taking the ratio of rms thermal fluctuations. We observe that as expected from Eq. (M4) for devices with higher coupling parameters, the ratio is closer to one [Fig. 18(c)]. One can also reverse Eq. (M4) and find the disorder parameter as a function of the asymmetry ratio:

$$\frac{\delta}{J} = \frac{1 - R^2}{2R}. \qquad (M5)$$

Using the linear relation found in Fig. 16(b), we can compute J from the geometric design parameters and translate Eq. (M5) to actual frequency and find the distribution of
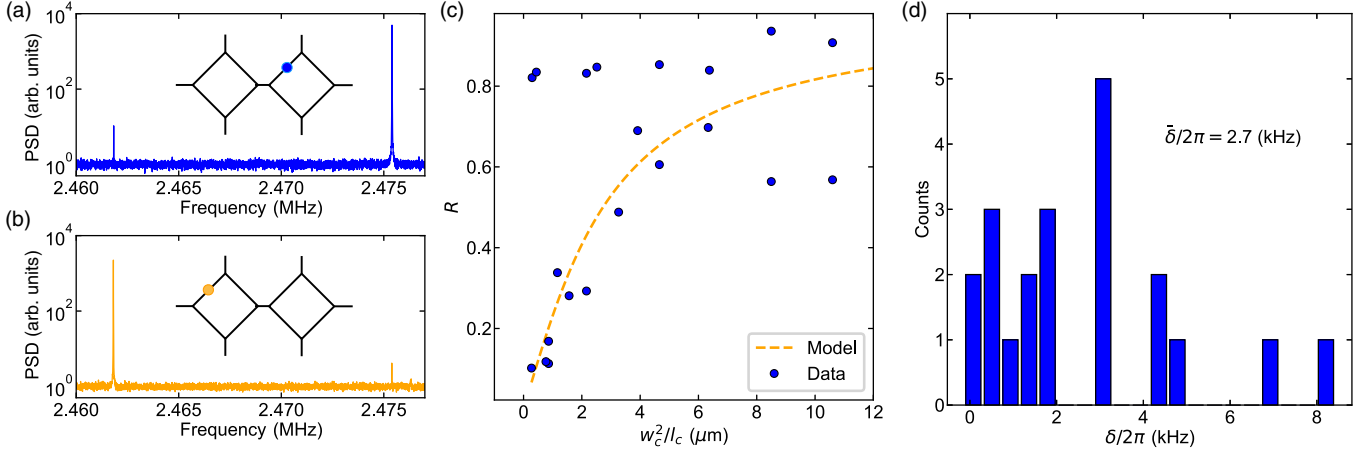
FIG. 18. Disorder in phononic dimers and arrays. (a),(b) Spectra of the interferometric measurement when the laser beam is focused on sides of the two resonators in a phononic dimer. The dimer's dimensions are similar to the ones shown in Fig. 6 with $w_c = 2.1$ μm and $l_c = 11.1$ μm corresponding to nominal frequency splitting of 1.1 kHz. (c) Asymmetry ratio [Eq. (M4)] obtained from the experimental spectra for devices with different coupling parameters, used for the measurement in Fig. 6(e). The dashed line is the model Eq. (M4) with δ set as its average value. (d) Histogram of the disorder parameter δ extracted from the data shown in (c) using Eq. (M5).

the disorder parameter for these devices. The histogram for δ is shown Fig. 18(d) and has an average around $\bar{\delta}/2\pi = 2.7$ kHz (equivalent to frequency splitting of 5.4 kHz). By plugging this average value into Eq. (M4) we can explain the average trend of the asymmetry ratio as a function of the coupling parameter [Fig. 18(c)]. These results explain the deviations from the FEM simulation in Fig. 6(e) for frequency splittings below 10 kHz as well as the localization in the edge modes of our phononic array [Fig. 6(h)].

APPENDIX N: COMPARISON OF POLYGON RESONATORS AND DOUBLY CLAMPED NANOBEAMS FOR INTEGRATION WITH WHISPERING GALLERY MODE OPTICAL CAVITIES

We use COMSOL to simulate the quality factor and effective mass of a 420-μm-long doubly clamped nanobeam with 20 nm thickness and 200 nm width with a single corrugation in the center of the nanobeam using a cosine profile to 600 nm over a 10 μm length. The corrugation was added to increase the optomechanical coupling rate. These design values are chosen as this geometry with 80 nm film thickness has been fabricated successfully with optical whispering gallery mode cavities [68]. For comparison, we consider a 20-nm-thick square resonator with $l_0 = 280$ μm and $r_l = 0.35$ (resulting in a clamp-to-clamp length of 420 μm). For the square sides, we use the same width profile as described for the nanobeam. The tether width is set to have a stress-preserving design similar to all the designs presented in this work. For the fundamental mode of the doubly clamped nanobeam, we find $Q = 6 \times 10^6$ and $f = 582$ kHz with effective mass of $m_{\text{eff}} = 2.7$ pg. The polygon resonator simulation results in the fundamental perimeter mode with $Q = 423 \times 10^6$ and $f = 863$ kHz with effective mass of $m_{\text{eff}} = 7$ pg. We estimate the optomechanical pulling factor G for each mechanical resonator using Eq. (2) of Ref. [19].

APPENDIX O: COMPARISON OF SYSTEM PARAMETERS FOR SIMILAR WORKS

In Table I we present the frequency, quality factor, effective mass and the thermal noise-limited force

TABLE I. Comparison of room temperature force sensing parameters for different types of mechanical oscillators.

References	Type	Frequency (Hz)	Q	Effective mass (kg)	$\sqrt{S_F}$ (N/$\sqrt{\text{Hz}}$)
Thompson *et al.* [72]	Membrane	1.34×10^5	1.1×10^6	4.0×10^{-11}	7.1×10^{-16}
Wilson *et al.* [40]	Membrane	9.00×10^5	4.0×10^6	8.4×10^{-12}	4.4×10^{-16}
Schmid *et al.* [38]	String	1.76×10^5	6.9×10^6	1.1×10^{-12}	5.4×10^{-17}
Reinhardt *et al.* [18]	Trampoline	4.09×10^4	4.5×10^7	4.0×10^{-12}	1.9×10^{-17}
Tsaturyan *et al.* [11]	Phononic crystal	7.77×10^5	2.1×10^8	1.6×10^{-11}	7.8×10^{-17}
Ghadimi *et al.* [15]	Phononic crystal	1.33×10^6	8.0×10^8	1.1×10^{-14}	1.4×10^{-18}
Bereyhi *et al.* [13]	Hierarchical	1.07×10^5	7.8×10^8	3.8×10^{-14}	7.4×10^{-19}
This work	Perimeter	3.50×10^5	3.6×10^9	1.7×10^{-14}	4.2×10^{-19}

sensitivity of a selection of uniform membranes, uniform strings, trampolines, phononic crystal beams and membranes, hierarchical beams and the perimeter modes presented in this work

———————

[1] G. I. González and P. R. Saulson, J. Acoust. Soc. Am. **96,** 207 (1994).

[2] M. Rossi, D. Mason, J. Chen, Y. Tsaturyan, and A. Schliesser, Nature (London) **563,** 53 (2018).

[3] D. J. Wilson, V. Sudhir, N. Piro, R. Schilling, A. Ghadimi, and T. J. Kippenberg, Nature (London) **524,** 325 (2015).

[4] D. Mason, J. Chen, M. Rossi, Y. Tsaturyan, and A. Schliesser, Nat. Phys. **15,** 745 (2019).

[5] J. D. Teufel, T. Donner, D. Li, J. W. Harlow, M. S. Allman, K. Cicak, A. J. Sirois, J. D. Whittaker, K. W. Lehnert, and R. W. Simmonds, Nature (London) **475,** 359 (2011).

[6] M. Aspelmeyer, T. J. Kippenberg, and F. Marquardt, Rev. Mod. Phys. **86,** 1391 (2014).

[7] L. Sementilli, E. Romero, and W. P. Bowen, Adv. Funct. Mater. **32,** 2105247 (2022).

[8] L. G. Villanueva and S. Schmid, Phys. Rev. Lett. **113,** 227201 (2014).

[9] S. A. Fedorov, N. J. Engelsen, A. H. Ghadimi, M. J. Bereyhi, R. Schilling, D. J. Wilson, and T. J. Kippenberg, Phys. Rev. B **99,** 054107 (2019).

[10] P.-L. Yu, T. P. Purdy, and C. A. Regal, Phys. Rev. Lett. **108,** 083603 (2012).

[11] Y. Tsaturyan, A. Barg, E. S. Polzik, and A. Schliesser, Nat. Nanotechnol. **12,** 776 (2017).

[12] M. J. Bereyhi, A. Beccari, S. A. Fedorov, A. H. Ghadimi, R. Schilling, D. J. Wilson, N. J. Engelsen, and T. J. Kippenberg, Nano Lett. **19,** 2329 (2019).

[13] M. J. Bereyhi, A. Beccari, R. Groth, S. A. Fedorov, A. Arabmoheghi, T. J. Kippenberg, and N. J. Engelsen, arXiv:2103.09785.

[14] D. Høj, F. Wang, W. Gao, U. B. Hoff, O. Sigmund, and U. L. Andersen, Nat. Commun. **12,** 5766 (2021).

[15] A. H. Ghadimi, S. A. Fedorov, N. J. Engelsen, M. J. Bereyhi, R. Schilling, D. J. Wilson, and T. J. Kippenberg, Science **360,** 764 (2018).

[16] S. Galliou, M. Goryachev, R. Bourquin, P. Abbé, J. P. Aubry, and M. E. Tobar, Sci. Rep. **3,** 2132 (2013).

[17] V. B. Braginsky, V. P. Mitrofanov, and V. I. Panov, *Systems with Small Dissipation* (University of Chicago Press, Chicago, 1985).

[18] C. Reinhardt, T. Müller, A. Bourassa, and J. C. Sankey, Phys. Rev. X **6,** 021001 (2016).

[19] R. Schilling, H. Schütz, A. H. Ghadimi, V. Sudhir, D. J. Wilson, and T. J. Kippenberg, Phys. Rev. Applied **5,** 054019 (2016).

[20] J. Guo, R. Norte, and S. Gröblacher, Phys. Rev. Lett. **123,** 223602 (2019).

[21] E. Gavartin, P. Verlot, and T. J. Kippenberg, Nat. Nanotechnol. **7,** 509 (2012).

[22] S. A. Fedorov, A. Beccari, A. Arabmoheghi, D. J. Wilson, N. J. Engelsen, and T. J. Kippenberg, Optica **7,** 1609 (2020).

[23] X. Li and Z. Liu, Solid State Commun. **133,** 397 (2005).

[24] T. Miyashita, J. Acoust. Soc. Am. **123,** 3039 (2008).

[25] N. D. Lanzillotti-Kimura, A. Fainstein, B. Jusserand, and A. Lemaître, AIP Conf. Proc. **1199,** 223 (2010).

[26] A. Khelif, A. Choujaa, R. Laihem, M. Wilm, S. Ballandras, V. Laude, and M. Solal, in *Proceedings of the IEEE Symposium on Ultrasonics, 2003* (IEEE, New York, 2003), Vol. 1, pp. 377–380, 10.1109/ULTSYM.2003.1293426.

[27] L. Catalini, Y. Tsaturyan, and A. Schliesser, Phys. Rev. Applied **14,** 014041 (2020).

[28] J. Košata, O. Zilberberg, C. L. Degen, R. Chitra, and A. Eichler, Phys. Rev. Applied **14,** 014042 (2020).

[29] D. Hälg, T. Gisler, E. C. Langman, S. Misra, O. Zilberberg, A. Schliesser, C. L. Degen, and A. Eichler, Phys. Rev. Lett. **128,** 094301 (2022).

[30] R. Süsstrunk and S. D. Huber, Science **349,** 47 (2015).

[31] L. M. Nash, D. Kleckner, A. Read, V. Vitelli, A. M. Turner, and W. T. M. Irvine, Proc. Natl. Acad. Sci. U.S.A. **112,** 14495 (2015).

[32] V. Peano, C. Brendel, M. Schmidt, and F. Marquardt, Phys. Rev. X **5,** 031011 (2015).

[33] J. Lu, C. Qiu, L. Ye, X. Fan, M. Ke, F. Zhang, and Z. Liu, Nat. Phys. **13,** 369 (2017).

[34] M. Miniaci, R. K. Pal, B. Morvan, and M. Ruzzene, Phys. Rev. X **8,** 031074 (2018).

[35] M. Schmidt, V. Peano, and F. Marquardt, New J. Phys. **17,** 023025 (2015).

[36] W. P. Su, J. R. Schrieffer, and A. J. Heeger, Phys. Rev. Lett. **42,** 1698 (1979).

[37] P. Neveu, J. Clarke, M. R. Vanner, and E. Verhagen, New J. Phys. **23,** 023026 (2021).

[38] S. Schmid, K. D. Jensen, K. H. Nielsen, and A. Boisen, Phys. Rev. B **84,** 165307 (2011).

[39] R. Groth and M. J. Bereyhi, *Fabrication of High-Aspect Ratio* Si_3N_4 *Nanobeam Resonators* (2020) 10.5281/zenodo.3898827.

[40] D. J. Wilson, C. A. Regal, S. B. Papp, and H. J. Kimble, Phys. Rev. Lett. **103,** 207204 (2009).

[41] A. Barg, Y. Tsaturyan, E. Belhage, W. H. P. Nielsen, C. B. Møller, and A. Schliesser, Appl. Phys. B **123,** 8 (2017).

[42] D. Rugar, H. J. Mamin, R. Erlandsson, J. E. Stern, and B. D. Terris, Rev. Sci. Instrum. **59,** 2337 (1988).

[43] J. V. Knuuttila, P. T. Tikka, and M. M. Salomaa, Opt. Lett. **25,** 613 (2000).

[44] M. Poggio, C. L. Degen, H. J. Mamin, and D. Rugar, Phys. Rev. Lett. **99,** 017201 (2007).

[45] P. R. Saulson, Phys. Rev. D **42,** 2437 (1990).

[46] P. F. Cohadon, A. Heidmann, and M. Pinard, Phys. Rev. Lett. **83,** 3174 (1999).

[47] O. Arcizet, P.-F. Cohadon, T. Briant, M. Pinard, and A. Heidmann, Nature (London) **444,** 71 (2006).

[48] M. Spletzer, A. Raman, A. Q. Wu, X. Xu, and R. Reifenberger, Appl. Phys. Lett. **88,** 254102 (2006).

[49] H. Okamoto, N. Kitajima, K. Onomitsu, R. Kometani, S.-i. Warisawa, S. Ishihara, and H. Yamaguchi, Appl. Phys. Lett. **98,** 014103 (2011).

[50] T. Faust, J. Rieger, M. J. Seitner, P. Krenn, J. P. Kotthaus, and E. M. Weig, Phys. Rev. Lett. **109,** 037205 (2012).

[51] R. B. Karabalin, M. C. Cross, and M. L. Roukes, Phys. Rev. B **79,** 165309 (2009).

[52] T. Ozawa, H. M. Price, A. Amo, N. Goldman, M. Hafezi, L. Lu, M. C. Rechtsman, D. Schuster, J. Simon, O. Zilberberg, and I. Carusotto, Rev. Mod. Phys. **91**, 015006 (2019).

[53] G. S. MacCabe, H. Ren, J. Luo, J. D. Cohen, H. Zhou, A. Sipahigil, M. Mirhosseini, and O. Painter, Science **370**, 840 (2020).

[54] A. Beccari, D. A. Visani, S. A. Fedorov, M. J. Bereyhi, V. Boureau, N. J.Engelsen, and T. J. Kippenberg, *Strained Crystalline Nanomechanical Resonators with Quality Factors above 10 Billion*, Nat. Phys. **18**, 436 (2022).

[55] M. Héritier, A. Eichler, Y. Pan, U. Grob, I. Shorubalko, M. D. Krass, Y. Tao, and C. L. Degen, Nano Lett. **18**, 1814 (2018).

[56] G. Gruber, C. Urgell, A. Tavernarakis, A. Stavrinadis, S. Tepsic, C. Magén, S. Sangiao, J. de Teresa, P. Verlot, and A. Bachtold, Nano Lett. **19**, 6987 (2019).

[57] Y.-T. Yang, C. Callegari, X. Feng, K. L. Ekinci, and M. L. Roukes, Nano Lett. **6**, 583 (2006).

[58] D. Hälg, T. Gisler, Y. Tsaturyan, L. Catalini, U. Grob, M.-D. Krass, M. Héritier, H. Mattiat, A.-K. Thamm, R. Schirhagl, E. C. Langman, A. Schliesser, C. L. Degen, and A. Eichler, Phys. Rev. Applied **15**, L021001 (2021).

[59] C. M. Pluchar, A. R. Agrawal, E. Schenk, and D. J. Wilson, Appl. Opt. **59**, G107 (2020).

[60] F. Tebbenjohanns, M. L. Mattana, M. Rossi, M. Frimmer, and L. Novotny, Nature (London) **595**, 378 (2021).

[61] A. H. Safavi-Naeini, S. Gröblacher, J. T. Hill, J. Chan, M. Aspelmeyer, and O. Painter, Nature (London) **500**, 185 (2013).

[62] T. P. Purdy, P.-L. Yu, R. W. Peterson, N. S. Kampel, and C. A. Regal, Phys. Rev. X **3**, 031012 (2013).

[63] V. Sudhir, D. J. Wilson, R. Schilling, H. Schütz, S. A. Fedorov, A. H. Ghadimi, A. Nunnenkamp, and T. J. Kippenberg, Phys. Rev. X **7**, 011001 (2017).

[64] N. Aggarwal, T. J. Cullen, J. Cripe, G. D. Cole, R. Lanza, A. Libson, D. Follman, P. Heu, T. Corbitt, and N. Mavalvala, Nat. Phys. **16**, 784 (2020).

[65] T. P. Purdy, R. W. Peterson, and C. A. Regal, Science **339**, 801 (2013).

[66] J. Cripe, N. Aggarwal, R. Lanza, A. Libson, R. Singh, P. Heu, D. Follman, G. D. Cole, N. Mavalvala, and T. Corbitt, Nature (London) **568**, 364 (2019).

[67] V. Sudhir, R. Schilling, S. A. Fedorov, H. Schutz, D. J. Wilson, and T. J. Kippenberg, Phys. Rev. X **7**, 031055 (2017).

[68] Measurement data and fabrication mask designs are available at https://zenodo.org, 10.5281/zenodo.6079845.

[69] T. Tian, Y. Ke, L. Zhang, S. Lin, Z. Shi, P. Huang, C. Lee, and J. Du, Phys. Rev. B **100**, 024310 (2019).

[70] S. A. Fedorov, A. Beccari, N. J. Engelsen, and T. J. Kippenberg, Phys. Rev. Lett. **124**, 025502 (2020).

[71] E. Gavartin, P. Verlot, and T. J. Kippenberg, Nat. Commun. **4**, 2860 (2013).

[72] J. D. Thompson, B. M. Zwickl, A. M. Jayich, F. Marquardt, S. M. Girvin, and J. G. E. Harris, Nature (London) **452**, 72 (2008).

Correction: The previously published Fig. 3 contained incorrect data in panel (c) and has been replaced. Corresponding changes to the caption have been made. The last sentence in the penultimate paragraph of Sec. III has been removed.